THESIS

LOW WORK FUNCTION, LONG LIFETIME FILAMENT FOR ELECTRON BEAM-BASED, WIRE-FED METAL ADDITIVE MANUFACTURING

Submitted by

Bao Gia Nguyen

Department of Mechanical Engineering

In partial fulfillment of the requirements

For the Degree of Master of Science

Colorado State University

Fort Collins, Colorado

Spring 2018

Master's Committee:

Advisor: Thomas Bradley
Co-Advisor: John Williams

Jose de la Venta Granda

ABSTRACT

LOW WORK FUNCTION, LONG LIFETIME FILAMENT FOR ELECTRON BEAM BASED, WIRE-FED METAL ADDITIVE MANUFACTURING

Tantalum filaments are used in electron beam additive manufacturing to thermionically emit electrons that are used to build near-net shape, metal parts. High operating temperatures are required to emit electrons which consequently limits the lifetime of these filaments. This thesis presents the thermionic emission characteristics of drop-in filament replacements that incorporate barium calcium aluminate cermets. Barium calcium aluminate is a low work function material used with hollow cathodes in electric propulsion devices to provide very long service lifetimes by acting as a moderate temperature, electron source. A marriage of these two technologies may limit downtime and increase the productivity and output of electron beam additive manufacturing.

Results of extended runtime tests are presented from configurations that immerse the modified filament in plasma and operate it as a vacuum emitter. The effect of contamination by air and fabrication methods are examined and evaluated based on effective work function and current density measurements. The latter includes formation methods for barium diffusion orifices as well as surface preparation methods for cermets. The experimental data collected were used to validate a predictive model that evaluates emission current densities, in both temperature and space-charge limited conditions, and effective work functions based on the fractional surface coverage of barium over a tantalum substrate.

ACKNOWLEDGEMENTS

I would like to express my gratitude to the members of my committee – my advisor Dr. Thomas Bradley, my co-advisor Dr. John Williams, and Dr. Jose de la Venta Granda. Their patience, accessibility, and enviable depth of knowledge have contributed significantly to my research, and their enthusiasm for all things engineering and science will have a lasting influence throughout my professional life.

I would also like to acknowledge Mrs. Daisy Williams and the close-knit group of students of the CEPPE lab who made my first experience working and learning in a laboratory setting an incredible one.

And special thanks to those who have given me valuable advice throughout my time as a graduate student. I'll be sure to step out of my comfort-zone more often and dial back – when reasonable – my obsession with perfectionism.

TABLE OF CONTENTS

ABSTRACT ii
ACKNOWLEDGEMENTS iii
LIST OF FIGURES v
1 INTRODUCTION 1
1.1 Wire-Fed, Electron Beam Additive Manufacturing 2
1.2 Thermionic Cathodes 9
1.2.1 Thermionic Emission 9
1.2.2 Directly Heated, Filament Cathodes 15
1.2.3 Low Work Function Cathodes 16
1.3 Low Work Function (LWF) Filaments 19
1.4 Thesis Outline 25
REFERENCES 26
2 METHODS AND MEASUREMENTS 29
2.1 Construction of LWF Filaments 29
2.2 Test Configuration 33
2.3 Procedures 39
2.4 Data Processing 43
2.5 Analytical Modeling 45
2.5.1 Transient Surface Diffusion and Emission Model for Hollow Cathodes 46
2.5.2 Transient Surface Diffusion and Emission Model for LWF Filaments 47
REFERENCES 50
3 RESULTS AND DISCUSSION 51
3.1 Extended Runtime Results 51
3.2 Comparison of LWF Filament Formation 56
3.3 Comparison to Analytical Model 63
3.4 Additional Observations 66
REFERENCES 68
4 CONCLUSION AND FUTURE WORK 69
4.1 Conclusion 69
4.2 Directions for Future Work 72
5 APPENDIX A: BAO-CAO-AL_2O_3 DECOMPOSITION 74
6 APPENDIX B: DIPOLE INTERACTIONS 77
7 APPENDIX C: MATLAB CODES 81
7.1 Calibration Code 81
7.2 Data Processing Code 82
7.3 Emission Model Parent Code 86
7.4 Emission Model Child Code 89
7.5 Emission Model Boundary Conditions Code 92

LIST OF FIGURES

Figure 1.1: Sciaky's EBAM 110 Additive Manufacturing System. 4
Figure 1.2: Schematic of a typical electron gun used in manufacturing applications [8]. 5
Figure 1.3: Sciaky's EBAM metal deposition process. 6
Figure 1.4: A typical tantalum filament used as an electron source for wire-fed EBAM systems. (a) is a brand new filament, (b) is a filament installed behind a Wehnelt cathode, and (c) is a filament that failed from material evaporation and thermal distortions. 7
Figure 1.5: An example of a simulated cathode activity curve generated in MATLAB. 14
Figure 1.6: Reproduced activity curves obtained for a dispenser type cathode [16]. 14
Figure 1.7: Emission current density (a) and evaporation rate (b) of select cathode materials [13]. (b) has been modified from its original form. 18
Figure 1.8: Cut-away of a LWF filament configuration. Centerlines indicate the location of barium diffusion orifices on the filament surface [27, 28]. 24
Figure 2.1: (a) The simplified formation process is capable of producing multiple inserts per batch. (b) and (c) provide close-up views of an insert that was faced on a lathe. 30
Figure 2.2: Low work function inserts: (a) as-fired, (b) dry-polished with sandpaper, and (c) ion-beam polished for 20+ hours. 31
Figure 2.3: The basket enclosure (a) around an insert and (b) assembled in a filament. 32
Figure 2.4: Filaments with holes that were either (a) mechanically drilled or (b) laser-burned. 32
Figure 2.5: The high density plasma source located on the right side (a) as it appears when it is rotated away from the filament to allow brightness temperature measurements, and (b) facing the electron gun during electron emission testing. 34
Figure 2.6: A schematic of the plasma generator and electron gun assembly is shown in (a) and their respective electrical schematics are shown in (b) and (c). 35
Figure 2.7: Schematic of the water-cooled anode and electron gun assembly is shown in (a), and its electrical schematic is shown in (b). 37
Figure 2.8: Vacuum emission testing configurations with the (a) anode assembly separated from the electron gun, and (b) fully assembled with a steel retaining ring securing the anode assembly to the gun body. 37
Figure 2.9: Power supply cabinet used with the vacuum emission testing configuration. 38
Figure 2.10: The disappearing filament wire runs vertically across the view window and appears directly in front of the test article positioned at the center of the gun. 42
Figure 2.11: Voltages (blue) and emissions (orange) from a LWF filament tested at 40 A. 44
Figure 2.12: A Schottky plot obtained from an unmodified, tantalum filament. 44
Figure 2.13: A diagram illustrating the simple distribution method used to determine electron emission from each diffusion orifice in the emitter. 49
Figure 3.1: SEM imaging of (a) un-tested and (b) tested ion-beam polished cermets sintered in air. The tested cermet was run for over 12 hours. 52
Figure 3.2: Plasma electron emission ('o') and heater current ('x') over a 75 hour extended runtime test with the emission threshold indicated by the bold line. 54
Figure 3.3: Vacuum electron emission measured at the end of an 8.5 hour test at 1000 V. 55

FIGURE 3.4: WORK FUNCTIONS OBTAINED FROM LWF FILAMENTS USING THE SCHOTTKY METHOD..... 57
FIGURE 3.5: EMISSION VARIANCE FROM FILAMENTS FORMED WITH LASER-BURNED AND MECHANICALLY DRILLED METHODS. BOTH WERE TESTED AT 500 V. 59
FIGURE 3.6: PHOTO SHOWING THE GAP BETWEEN THE DETACHED TANTALUM FOIL BASKET AND FILAMENT THAT ALLOWED THE ESCAPE OF BARIUM VAPOR. 59
FIGURE 3.7: EMISSION VARIANCE BETWEEN AS-FIRED, ION-BEAM POLISHED, AND DRY-POLISHED SURFACE FINISHES ON CERMETS. 61
FIGURE 3.8: EMISSION VARIANCE IN AN AS-FIRED CERMET AFTER TWO EXPOSURES TO AIR..... 63
FIGURE 3.9: EMISSION CURRENT DENSITY DATA POINTS COLLECTED AT 500 V OVERLAID ON THE MATLAB MODEL. 65
FIGURE 6.1: A SCHEMATIC ILLUSTRATING VALENCE ELECTRON INTERACTIONS IN $Ba^{+}O^{-}$ DIPOLES. 78

1 Introduction

The potential of additive manufacturing (AM) to disrupt the status quo of conventional manufacturing and bring rapid production to industry has been a well-known and often discussed topic for years, and its steady encroachment is difficult to ignore. The research and subsequent innovation activities that have allowed this market penetration continue to advance the sophistication of AM technologies. The suite of print-compatible materials has swelled from its early focus on thermoplastics to include pure metals and alloys and recently has begun to establish a presence with ceramics and composites. AM technologies that are now commercially available in a variety of configurations were born from this research, including mainstays like material extrusion, powder bed fusion (PBF), and directed energy deposition (DED). This versatility in both material compatibility and unit configuration has allowed AM to carve a niche in markets ranging from consumer level hobbyists to research institutions to large manufacturing industries, and it continues to grow. The AM industry has experienced significant revenue increases over the past several consecutive years. In 2015 revenues from the sale of AM capital products totaled $2.3 billion after growing 28.8%, 41.3%, and 31.6%, and 18.4% between 2012 and 2015. AM related services totaled $2.8 billion after experiencing similarly strong growths of 36.4%, 26.3%, 38.9%, and 33% between 2012 and 2015 [1]. As research continues to improve on the versatility of AM technologies, its expanding presence within current markets may be complemented by its adoption in other industries.

Wire-fed, electron beam-based systems, known also as Electron Beam Freeform Fabrication (EBF^3), used for additively building metal parts are one such candidate that

may see wider adoption as a faster, more cost-effective alternative to conventionally made castings and forgings. The successful introduction of EBF^3 into other industries may be hindered though by the frequent replacement of electron gun filaments, a critical component in EBF^3 machinery, whose relatively short lifetime limits the run-time allowance of the equipment. This paper presents the work put forth to develop and test solutions for this production-limiting component.

1.1 Wire-Fed, Electron Beam Additive Manufacturing

EBF^3 is a process within the additive manufacturing subclass of directed energy deposition technologies that utilizes a focused, high energy electron beam in a vacuum environment to locally melt a metal substrate in which wire feedstock made from a variety of metal alloys is injected. It is characterized by high metal deposition rates and low material waste. EBF^3 has been the focus of study by several researchers since 1995 with a substantial amount contributed by Karen Taminger and Robert Hafley at the NASA Langley Research Center [2, 3, 4]. There, they investigated the mechanical properties of parts made from various metal alloys through the EBF^3 process and found that, for titanium and aluminum, they were able to achieve a wide range of mechanical properties and microstructures comparable to the their wrought form [2]. Taminger et al. concluded that EBF^3 can provide a cost-effective and shorter lead-time alternative to conventional castings and forgings in the near-term and offer tailored unitized structures with functionally graded microstructures and compositions that promote improved structural efficiencies in the future [2]. Gibson et al. echoed this when they noted that DED AM technologies, like EBF^3, are increasingly used to produce near net structures in place of wrought billets. They went on to add that this application of the technology is complemented by its ability to

repair and append features to existing structures to extend life and improve performance characteristics [5].

EBF^3 primarily maintains a presence within the aerospace industry where it is used to print and repair aircraft frames, structures, and parts through third-party services and in-house operations. In 2009, Sciaky, a company that manufactures capital equipment and provides services for electron beam welding, became the first known producer of commercially-available, EBF^3 units branded as Electron Beam Additive Manufacturing (EBAM) and began partnerships with prominent organizations within the aerospace and defense manufacturing sectors. Sciaky released a case study that exemplified EBAM's manufacturing efficiencies for a project that produced a titanium propellant tank for Lockheed Martin Space Systems. In it, Sciaky reported that the time required to manufacture the tank was reduced by 80% compared to conventional means at 45% of the cost [6]. Frazier compiled data from other researchers that reported similar cost savings for EBF^3 ranging from 30% to 44% [7].

EBAM systems consist of a large vacuum chamber capable of reaching pressures below the 10^{-4} Torr range, an internally mounted, electronically-controlled, electron gun assembly, and an internally-located, one- or two-wire feed system. The orientation and position of the electron gun and wire feed assembly are independently controlled to allow printing of complex shapes. The wire feed system is able to accommodate different wire gauges and metal allowing for fine and coarse feature depositions and compositional gradients for metals including titanium, tantalum, tungsten, aluminum, and various steels. Figure 1.1 shows the general size of an EBAM unit and the arrangement of systems and assemblies inside the vacuum chamber.

Figure 1.1: Sciaky's EBAM 110 Additive Manufacturing System.

A cross-sectional schematic of an electron gun is shown in Figure 1.2 and is comprised of a filament, a cathode, an aperture anode, and focusing and deflection coils. The filament and cathode, also called a Wehnelt cylinder or focusing cup, are mounted within the ceramic gun cap and electrically insulated from each other and the rest of the gun assembly. Two power supplies connected to the filament provide (1) electrical current up to 75 A to heat the filament and (2) a negatively biased voltage up to 60 kV relative to ground to accelerate electrons from the filament. A third power supply controls the voltage of the cathode. It is used to bias the cathode negative of the filament by up to 1000 V. The deflection and focus coils are controlled by their own power supplies while the anode and the rest of the assembly are grounded.

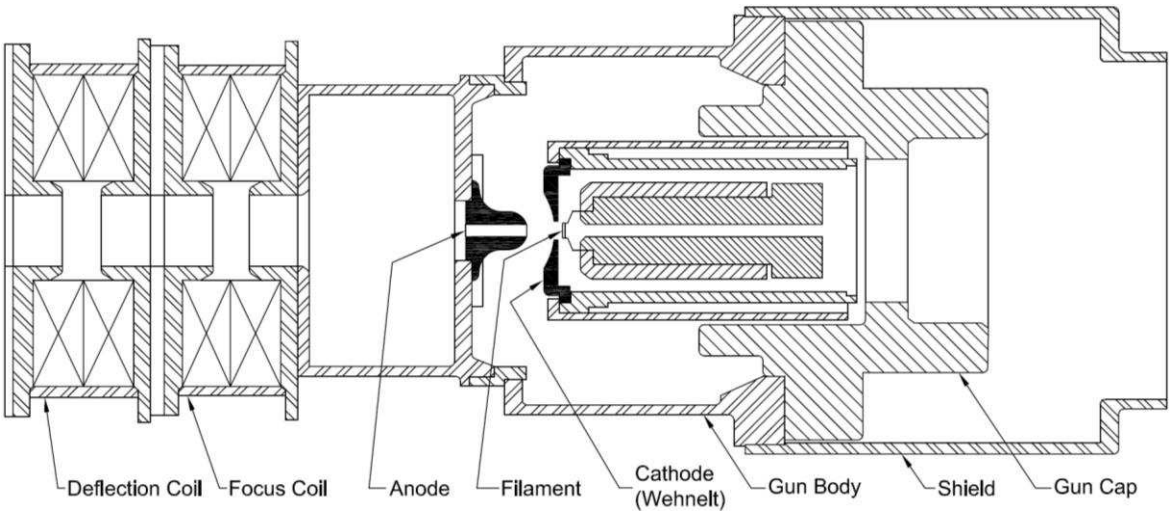

Figure 1.2: Schematic of a typical electron gun used in manufacturing applications [8].

Electron beams are generated by the gun assembly through the acceleration and focusing of thermionically emitted electrons sourced from the filament. The filaments used in wire-fed AM applications are made from .005” or .007” thick tantalum foil formed into a button-shaped, planar surface approximately .175” in diameter (see Figure 1.4(a)) that act as the emitting surface or area. The filament legs leading to and from the emitting area are used to connect the filament to electrodes. During a printing campaign, a DC current of 60-75 A flows through the filament legs to resistively heat it to operating temperatures between 1825°C and 2225°C where electrons are emitted thermionically. A potential difference, or accelerating voltage, between the filament and anode of 40-60 kV is used to accelerate the electrons from the filament and through the anode and coils downstream. The cathode, featuring a prominent dish and centrally located aperture, is shaped to produce an electric field that focuses the accelerated electrons right as they leave the filament creating a favorable initial velocity condition, which allows the beam to pass through the aperture anode with minimal impingement. The cathode also functions as an

emission suppressor regulating the amount of current emitted from the surface of the button filament by varying its non-zero, negative bias up to 1000 V to a beam current between 200 and 250 mA (approximately 1.29–1.61 A/cm^2). If the cathode is not biased, the maximum temperature or space-charge limited emission is delivered. The cathode's aperture, as shown in Figure 1.4(b), is centered over the filament with a clearance of approximately .080" on the diameter, and the base of the dish is positioned approximately .020" in front of the filament's planar surface. The electron beam is refocused as it leaves the gun assembly by a first stage of coils and is steered by a second stage of coils to manipulate its exit angle and heat a controlled area on the work piece. The feed system deposits metal alloys onto the work piece by injecting wire through a nozzle into the heated area at rates between 7–20 lbs. per hour. A near-net shape part slowly emerges as the gun assembly and wire-feed system move through the chamber, heating and depositing metal, layer by layer. The parts that finally emerge typically require post-process machining to meet the dimensional requirements of the component. Figure 1.3 illustrates this deposition process.

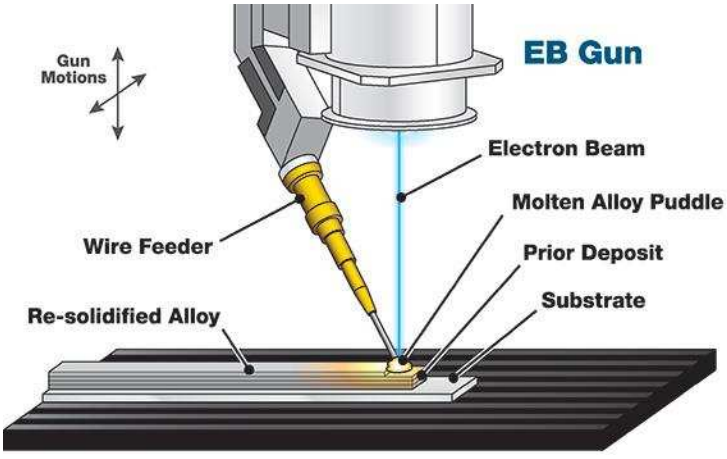

Figure 1.3: Sciaky's EBAM metal deposition process.

Printing time is limited by the lifetime of the filament, which may fail as a result of excessive material loss or with the onset of vacuum arcs. As electrons are extracted over time, the emitting area slowly evaporates and sputters and one of two things may happen: the filament may continue to evaporate until a break forms creating an open circuit or microscopic pockets created by evaporating or sputtering tantalum forms a surface blemish significant enough to act as an arc initiation site. At the same time, the high temperatures necessary to sustain a minimum emission current may cause grain growth within the tantalum eventually distorting the shape of the filament. Movement caused by distortion can result in reduced spacing between the filament and the closely neighboring cathode and causing increased localized electric fields that initiate arcs. The filament end-of-life due to material evaporation or dimensional distortions typically occurs after 4 to 12 hours of use, skewing predominately towards the shorter lifetime. Figure 1.4(c) is a photograph of a tantalum filament that underwent a 13-hour printing campaign before failing. The image was captured using a Vision Engineering Mantis Elite stereo microscope at a magnification of 10x and shows both distortion and surface erosion of the filament.

(a) (b) (c)

Figure 1.4: A typical tantalum filament used as an electron source for wire-fed EBAM systems. (a) is a brand new filament, (b) is a filament installed behind a Wehnelt cathode, and (c) is a filament that failed from material evaporation and thermal distortions.

To resume production once a filament has reached its end-of-life, the vacuum chamber must be vented, a new filament must be installed, and the chamber must be pumped down back to the appropriate vacuum conditions. This process can take up to 24 hours to complete before a printing campaign may resume resulting in lost production time. The interruption can then reverberate to downstream manufacturing processes such as finish-machining and assembly and become detrimental to production schedules that seek to capitalize on the condensed lead times and reduced manufacturing costs offered by EBF^3 and EBAM.

Extending the lifetime of filaments is a solution that would increase productivity of EBAM systems while concurrently adding value to the capital investments made by customers in the technology. A demonstrable improvement in the run-time allowance, in addition to the existing advantages of cost and lead-time savings, may entice companies outside of the aerospace industry to adopt EBF^3 for their casting and forging requirements as well. The value of a long-lifetime filament would not be restricted to just EBF^3/EBAM either. Its cross-industry application could beneficially impact welding, semiconductor manufacturing, and ion beam etching processes that utilize filaments in electron beam guns, physical vapor deposition systems, and plasma bridge neutralizers.

Increasing filament lifetime can be accomplished by recognizing that the root of filament failure originates from the high heat input and temperature required to enable thermionic electron emission. By reducing of the filament's work function through the introduction of a low work function insert, the DC currents required to emit electrons from the filament would be lowered, and consequently the heat load placed onto the filament would decrease along with its temperature. This would retard the onset of thermally-

induced, geometric distortions and material evaporation. The work presented in this thesis aims to reduce the existing DC heating currents from 60–75 A to under 40 A while maintaining a 200 mA beam current and increase the run-time allowance to 50 hours and beyond. A model used to predict emission from a low work function filament and aid in the refinement of its design is also developed and presented. An overview of fundamental concepts related to thermionic cathodes critical to the development of this solution follows.

1.2 Thermionic Cathodes

Thermionic cathodes and the physics that describe their behavior are well-understood topics that have resulted in the maturation of cathode technology and its inclusion in a wide range of devices. These cathodes are at the core of many devices used in manufacturing, aerospace, and research. Medical x-ray imagers, scanning electron microscopes, electron beam welders, sputter deposition and ion beam etching systems, traveling wave tubes, and electric thrusters for satellites represent a sampling of current technology utilizing some form of thermionic cathode. Up until the 1990s filament-type, thermionic cathodes were ubiquitously found in cathode ray tube (CRT) televisions and computer monitors.

1.2.1 Thermionic Emission

Thermally inducing the emission of electrons from the surface of a material is known as thermionic emission and is typically accomplished by resistively heating an electron source - usually a filament. A potential difference between the emitting surface and a downstream anode can then be used to extract and accelerate electrons. These

primary electrons can be focused into a beam for use in applications such as additive manufacturing devices or used to bombard inert or reactive gas to create plasma.

The value of the energy required to induce the emission of an electron is known as the work function and is dependent on the material used as the electron source and its surface conditions. The work function is formally defined as the minimum amount of energy, measured in electron-volts (eV), required to displace electrons to a location in vacuum immediately adjacent to the source or emitting surface. The work function can be altered significantly through surface-level, molecular processes. The selection of materials and surface modifications with low work function is of paramount importance for devices relying on thermionic electron emission at moderate temperature.

Thermionic cathodes operate within distinct regions that are dependent on the temperature of the cathode, its distance from the anode, and voltage difference between the electrodes. The emission current density, or the electron emission rate per unit area of the emitting surface, of thermionic cathodes in the temperature limited or space-charge limited conditions is described by the Richardson-Dushman equation and Child-Langmuir Law, respectively.

The temperature limited (TL) condition of thermionic emitters is a regime in which the exponential increase in current density is limited by the temperature of the cathode. The Richardson-Dushman equation for the current density of an emitter is defined by Equation 1.1, where j_{TL} is the emission current density of electrons in A/m^2, "A" is the Richardson constant equal to 1,201,730 A/m^2K^2, γ_r is a material-specific reflection coefficient, T is the temperature of the cathode in Kelvin, e is the magnitude of the charge of an electron in coulombs, ϕ is the work function of the emitter in eV, and k is Boltzmann's

constant in J/K. It is important to note that the TL current density is solved using a single valued work function over the entire area of the emitting surface. Because the work function is a dependent on the surface condition of the emitter and not of its bulk material, localized variations of the work function can be present on the emitter's surface [9, 10]. Therefore throughout this paper, the effective work function will be implied in all references to work function unless otherwise noted or discussed.

$$j_{TL} = A\gamma_r T^2 exp\left(\frac{-e\phi}{kT}\right) \tag{1.1}$$

Thermionic electron emission can be enhanced through the Schottky effect, which reduces the work function of the emitter in the presence of an electric field. The Richardson-Dushman equation can be modified to account for the field-enhanced, thermionic emission and is defined by Equation 1.2, where ϵ_o is the vacuum permittivity in F/m, and E is the electric field in V/m near the emitter. The electric field can be determined by considering the potential difference and gap between the emitter and anode.

$$j_{TL} = A\gamma_r T^2 exp\left(\frac{-e\phi}{kT}\right) exp\left(\frac{e}{kT}\sqrt{\frac{eE}{4\pi\epsilon_o}}\right) \tag{1.2}$$

The exponential increase in electron current density with temperature for thermionic emitters operated at a constant electric field condition does not continue indefinitely. Rather the current density begins to plateau and saturate and is said to be space-charge limited (SCL) once the current density approaches a critical value. In this condition any further increase in cathode temperature does not result in increased emission. Space-charge limitations arise due to the accumulation of electrons adjacent to the emitter that form a negatively charged region that reduces the electric field at the

emitter surface. The charged region repels electrons back to the thermionic emitter only allowing some to be extracted and accelerated to an anode. Space-charge and its effect on reducing the electric field at the emission electrode is more pronounced at higher temperatures due to the greater accumulation of electrons from thermionic emission compared to the field that exists at lower temperatures where relatively low electron space-charge occurs [11, 12, 13]. The effect of space-charge on electron emission has been reported to extend to as low as 5% of the SCL emission current limit, which essentially causes some space charge limitation effects within the predominately temperature-limited condition [10]. Emission current density at the SCL is a function of the potential difference, V, and distance, d, between the cathode and anode and is approximated by the one-dimensional Child-Langmuir Law defined in Equation 1.3. Equation 1.3 assumes the cathode and anode can be represented as two infinite parallel plates. Note that for a given cathode temperature in the SCL region, the current density is highly space-charge limited at lower voltages and greater electrode spacings. Space-charge limitations can be reduced and observable emission can be increased with the application of higher voltages and through the use of smaller electrode gaps.

$$j_{SCL} = \frac{4}{9}\epsilon_o \sqrt{\frac{2e}{m_e}} \frac{V^{3/2}}{d^2} \tag{1.3}$$

Figure 1.5 contains an activity curve for a filament cathode that was constructed from using the Richardson-Dushman equation and Child-Langmuir Law. The activity curve was generated in MATLAB and used to predict the performance of cathodes over a range of parameters. The code automatically converted the current density solution from the Richardson-Dushman equation and Child-Langmuir Law to an emission current based on

the area of the emitting surface. This current is plotted against the cathode brightness temperature. The code will be discussed later in this paper, and the script in its entirety can be found in Appendix C. The simulated activity curve solves for emission from both TL and SCL regimes separately and illustrates the exponential increase with temperature for the TL curve and the constant emission for a given accelerating voltage and filament-anode gap in the space-charge limited region. The intersection of the TL and SCL emissions is referred to as the kneepoint [14, 15], and for a particular cathode, its migration towards higher temperatures over time for a given current density is indicative of the cathode's increasing work function [9] and degrading performance. If a plot is generated tracking the temperature associated with the kneepoint over time, a trend for a particular cathode will emerge allowing an estimation to its performance in the future [9, 14].

The kneepoint, however, is not an observable phenomenon in practical performance evaluations of thermionic cathodes. As it was previously mentioned, the exponential increase of the TL region gradually transitions to the plateaued emission of the SCL region in what is referred to as the SCL-TL knee. The knee can be attributed to variations in localized surface work functions (in contrast to the Richardson-Dushman equation that uses a single-valued, effective work function) and the dependency of perveance on the anode-cathode spacing as it is affected by the increasing cathode temperature [9, 10]. The variations in work function, due in part to either cathode poisoning or incomplete thermal activation, affect the degree of roundness in the SCL-TL knee as well, which becomes more pronounced with increasing current densities and voltages [9]. The plot in Figure 1.6 was reconstructed from data collected by Vancil et al. and illustrates the changing shape of the SCL-TL knee with increasing voltage for a dispenser type cathode [16].

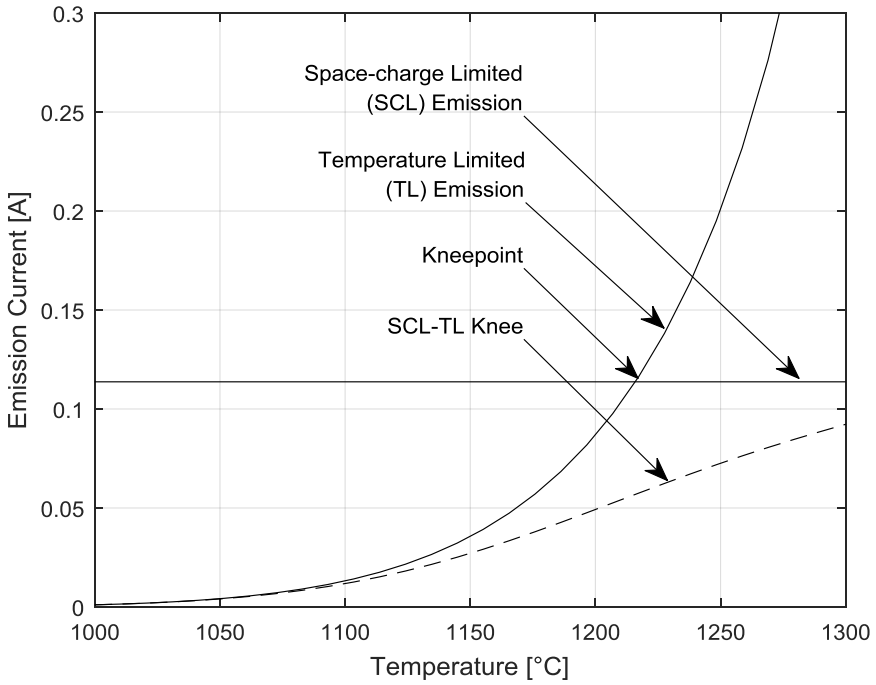

Figure 1.5: An example of a simulated cathode activity curve generated in MATLAB.

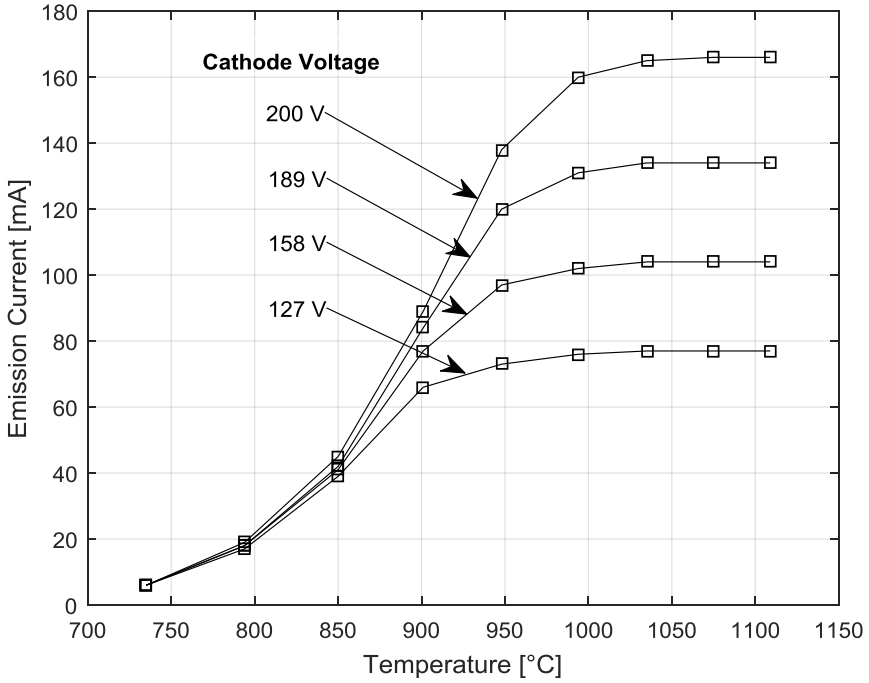

Figure 1.6: Reproduced activity curves obtained for a dispenser type cathode [16].

1.2.2 Directly Heated, Filament Cathodes

Directly-heated, filament cathodes, like the familiar coil filaments found in antiquated incandescent light bulbs, preceded the use of low work function (LWF) cathodes in electron and ion sources. Many of these directly-heated filaments were made from tungsten and tantalum wires and suffered from accelerated deterioration due to high operating temperatures much like the button filaments used in EBF^3/EBAM. These types of cathodes, with work functions of ~4.2 eV for tantalum and ~4.5 eV for tungsten, had to be elevated to temperatures ranging from 2200–2250°C and 2350–2370°C, respectively, to yield an emission density in the 1 A/cm^2 range [13, 17]. Sustaining such high temperatures led to the rapid evaporation of the filament material. Tungsten, operating with a 1 A/cm^2 load, would evaporate at a rate of ~5 x 10^{-7} gm/cm^{2}s, which would increase if greater current densities were required [13]. This high rate of evaporation limits the lifetime of tungsten filaments to 100 hours or less [13]. In some applications where filament cathodes were used in ion sources and plasmas were present during operation, the deterioration of filaments would be exacerbated by the bombardment of positively-charged ions such that lifetimes were typically less than tens of hours.

Early solutions to extend the lifetime of wire filament cathodes were proposed, however they were either susceptible to the same failure mechanisms or required greater electrical resources reducing the overall efficiency of the device. Kaufman et al. noted that low work function coatings applied to filaments would reduce the heating power required. Unfortunately, these coatings were relatively quickly sputtered off [17]. Using larger diameter wire filaments was also suggested, and while it was found that filament lifetimes increased linearly with the diameter, the currents needed to heat the wire to an

appropriate temperature increased as well, which required high current power supplies and large diameter electrical leads. Ehlers et al. reported that for a .010" diameter tungsten wire, 8–9 A were required to raise the temperature of the filament to 2350°C. The heating current nearly doubled to ~20 A for a .020" diameter wire and increased to ~95 A for a .060" diameter wire [18].

1.2.3 Low Work Function Cathodes

The high operating temperatures, current density limitations, and short lifetimes of directly heated filaments invariably led to the development of low work function cathodes. Chief among these were those that relied on the diffusion of molecules over the cathode's emitting surface to reduce its overall work function. Known as dispenser cathodes, these diffusion-based devices are further subdivided into impregnated and reservoir type cathodes [19], and their ongoing development since the 1960s has already produced cathodes that operate at lower temperature, throttle evaporation rates of the electron source material, extend lifetimes by 1000 times, and yield greater electron current densities. Consequently devices such as Hall-effect and ion thrusters, neutralizers, and terrestrial plasma electron sources have included LWF cathodes to exploit their capability to produce current densities greater than 10 A/cm^2 with lifetimes on the order of tens of thousands of hours.

The low work function cathodes described herein rely on the surface diffusion of barium atoms, which are sourced from an insert, to coat the emitting surface of the cathode and reduce its overall work function to ~2.1 eV. In operation the insert, composed of a porous tungsten matrix impregnated with a barium calcium aluminate ($BaO\text{-}CaO\text{-}Al_2O_3$) ceramic compound, is resistively heated to a temperature between ~1000-1200 °C. The

elevated temperature initiates chemical reactions within the ceramic compound and releases barium and barium oxide vapor that then migrates through the porous structure of the tungsten matrix. Free barium forms a dipole with oxygen ($Ba^{+}O^{-}$), which has adsorbed to the tungsten substrate with its own dipole ($W^{+}O^{-}$), and creates a dipole monolayer over the surface of the emitter. The $Ba^{+}O^{-}$ dipole that forms over these surfaces can reduce the work function of the tungsten substrate to as low as ~2 eV [20]. Some barium is lost to evaporation; however the emitter surface is continually replenished with barium until the impregnated insert is exhausted of the barium ceramic compound.

Decades of research have been dedicated to the development of barium calcium aluminates, generically referred to as barium ceramics or compounds, and the porous tungsten metal matrix, which provides both the structure for the insert and aids in the decomposition and dispensing of barium from the ceramic [21]. Three commonly used variations of the barium compound emerged and are typically referred to by their respective molar ratios of BaO, CaO, and Al_2O_3 as 5:3:2, 4:1:1, and 3:1:1. Cathodes that incorporate inserts with 5:3:2 and 4:1:1 compositions are also referred to in the literature as B-type and S-type cathodes. Despite the different amounts of the constituent ceramics, which attempt to exploit the stabilizing effect of alumina (Al_2O_3) on barium oxide's hygroscopic nature and calcium oxide's ability to reduce the barium sublimation rate and enhance emission, the three formulations share work function within ~0.1 eV of each other [22]. The effect of barium ceramics on lowering work function enable them to be used to produce current densities from 1–10 A/cm^2 between temperatures of ~1000-1200 °C compared to tungsten and tantalum which yield comparable current densities at temperatures between ~2350-2700 °C and ~2200-2500 °C, respectively. Figure 1.7(a)

illustrates the favorable current density of the 4:1:1 barium ceramic as a function of temperature relative to pure tungsten and tantalum emitters as well as to lanthanum hexaboride (LaB_6), another LWF emitter with a work function of 2.8 eV [23]. High current densities at comparatively low temperatures for barium compounds have the effect of reducing the material's evaporation rate and subsequently extending the overall operating lifetime of the cathode. The improvement is immediately apparent in Figure 1.7(b) when compared to pure tungsten emitters, and while cathodes utilizing boride ceramics evaporate at slightly slower rates than barium ceramics, the higher emission temperatures required for LaB_6 reduce this benefit. Forman and Smith performed life tests on various dispenser cathodes, which included the 4:1:1 S-type and 5:3:2 B-type compositions. At cathode loads of 2 A/cm^2, they reported that the S cathode was able to operate for 20,000 hours while the B cathode reached in excess of 30,000 hours and continued on past the publication of their studies [24]. Cronin later reported that the B cathodes continued operating past 50,000 hours [22].

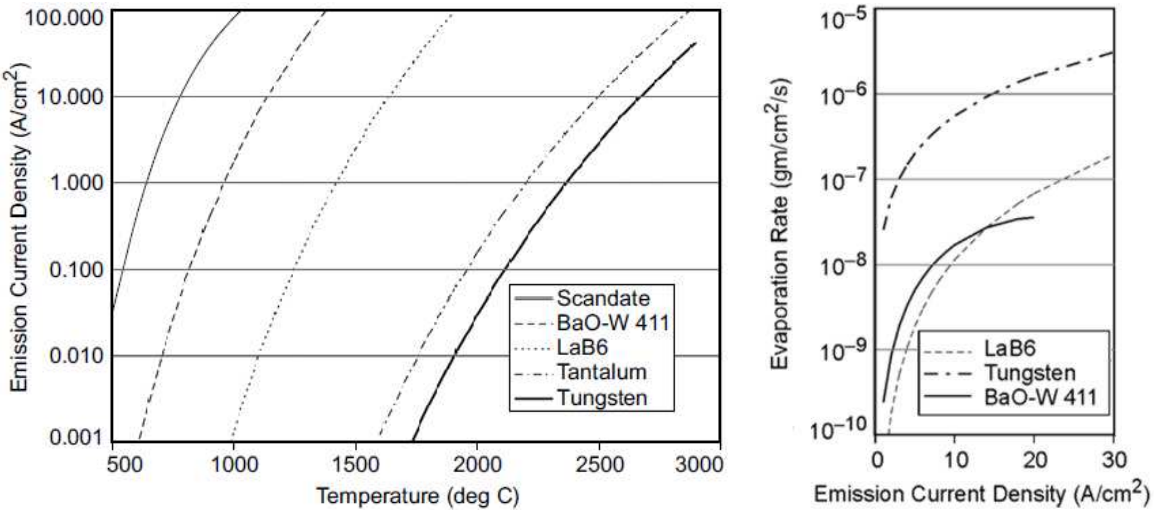

(a) (b)

Figure 1.7: Emission current density (a) and evaporation rate (b) of select cathode materials [13]. (b) has been modified from its original form.

The demonstrable performance of LWF cathodes as well as the flexibility in size and shape of the impregnated inserts and the diffusion and dipole mechanisms that allows barium to coat metal substrates creates a versatile delivery system adaptable to other cathode geometries.

1.3 Low Work Function (LWF) Filaments

The marriage of low work function, impregnated inserts to filaments used in electron beam additive manufacturing offers the potential to extend their longevity and increase the run-time allowance of EBAM units but is complicated by factors including preparation of a cost-effective impregnated insert, controlled dispensing of barium, and reconciling the interactions of a LWF filament on an existing electron gun assembly that is controlled by algorithms developed for prompt emitters.

As it was described earlier, filaments currently used in EBAM equipment have issues operating for longer than 4 hours because of material evaporation or shape distortion issues that ultimately lead to the filament's failure. The root of these failures can be traced back to the relatively high work function of the tantalum filament (~4.2 eV) and the high temperatures that tantalum requires (~2200-2500 °C) to emit electrons thermionically. One solution would be to reduce its work function with the use of a barium calcium aluminate insert, which would allow the filament to emit comparable current densities at lower operating temperatures. This would eliminate most of the root causes that lead to filament failures and, consequently, extend its lifetime. Precedence has been established as to the applicability of LWF inserts with cathodes similar to the filaments used in EBAM. In terms of the metal substrate used for the diffusion of barium molecules, much of the discussion up to this point has focused on tungsten as the primary material of these

emitting surfaces; however, many existing cathodes, especially hollow cathodes, are regularly made from both tungsten and tantalum eliminating concerns of $Ba^{+}O^{-}$ and $Ta^{+}O^{-}$ dipole incompatibility. In addition, while the discussion of LWF cathodes began by listing devices that used emitted electrons to produce plasmas, these cathodes also have been used as emitters in vacuum devices such as the traveling wave tube [25]. The versatility of LWF cathodes in this regard is important since filaments used in EBAM operate in similar conditions as vacuum emitters – without the presence of inert gases or plasmas.

Although barium ceramic inserts can be used to reduce the work function of tantalum filaments, the formation of commercially-produced, impregnated inserts is a manufacturing-intensive and time-consuming process that results in a relatively expensive final product compared to the cost of a filament. The formation process involves pressing and sintering tungsten powder into billets and then infiltrating the billet with plastic to preserve the porous surface and interior from damage during machining operations. Once the billet is machined to an appropriate shape for the cathode, the plastic filler is removed from the porous metal matrix using an air-fired furnace and is replaced with the barium ceramic compound through an impregnation process performed in a hydrogen furnace. There is no direct control to ensure that the ceramic has uniformly infiltrated the porous matrix; however the insert is weighed before and after the process to determine how much of the ceramic was impregnated into the porous tungsten. Some formation processes include a finish machining operation of the emitting surface that potentially smears tungsten over surface level pores inhibiting the diffusion of barium. This may be rectified through a final cleaning process that involves either grit blasting or lightly sanding the insert with alumina [10, 22, 26].

Procuring a number of inserts for testing much less providing a cost-effective, low work function solution would be untenable if commercially sourced. Fortunately, an existing partnership with Plasma Controls LLC, a local company in Fort Collins who has exclusively licensed the patented Colorado State University cermet formation technology and specializes in manufacturing hollow cathodes and plasma diagnostic tools, has collaborated with us in the production of LWF inserts. The method is a mix and sinter process that produces a distinct type of insert in the form of a ceramic-metal (cermet) composite [27, 28]. The cermet insert can be formed to any desired shape and size with little or no post-process machining, enables greater control over the uniformity of the barium ceramic compound throughout the insert, and allows for convenient experimentation with different cermet compositions including variants to the barium ceramic formulation, ceramic-to-tungsten weight ratios, and tungsten particle sizes.

This research explores the use of cermets made with the standard 5:3:2 barium ceramic formulation and trace amounts of scandate and other constituents. Because these inserts are formed with a fundamentally different method than commercially-made impregnated cathodes, these cermets will not be referred to as B-type cathodes. Early tests investigated the effect on emission of using fine and coarsely-sized tungsten powder for the porous matrix and sintering the ceramic-tungsten mixture at atmospheric pressure and at vacuum. It was made apparent that vacuum-fired cermets or those made with coarse tungsten powder yielded poor emission compared to the atmospheric pressure furnace alternative. As a result, subsequent tests used these cermets made with fine tungsten powder. The effect of surface finish on emission was also explored.

Non-uniformity in the barium monolayer can negatively affect the overall work function of a cathode and ultimately the emission it can yield, and while this can be caused by irregular or restricted delivery of barium vapor from the insert [10] or localized poisoning through the formation of unfavorable dipoles on the emitting surface (see Appendix B), long diffusion lengths from the source of barium to the surface can contribute significantly to incomplete surface coverage. A number of solutions to this issue have revolved around the controlled dispensing of barium through perforations made to the emitting surface of a cathode. These are referred to as controlled porosity dispenser (CPD) cathodes, and in one of the earliest embodiments of a CPD cathode, Falce and Thomas chemically etched an array of holes in molybdenum foil that was coated with iridium. The foil was placed in front of a tungsten impregnated cathode to act as both an emitter and to control barium diffusion [29]. More recently Ives et al. at Calabazas Creek Research developed an improved CPD-based emitter for reservoir cathodes [26] through a comparatively more involved process. Manufacturing the emitter required sintering several layers of tungsten wire wrapped around a spool and using electrical discharging machining to shape the bonded structure into an emitter cap. In both cases, CPD cathodes showed favorable results. Ives et al. provided a comparison of their sintered tungsten wire emitter to a best of class B-type cathode operated at 4 A/cm^2 and reported that the CPD emitter improved on the cathode work function by 2% [30].

A similar, simplified method to that of Falce et al. was incorporated into the planar filaments using an array of holes, or diffusion orifices, to control barium coverage by varying their quantity, size, and location; however, none of the configurations tested included any type of supplemental coating, such as iridium, on the emitting surface. The use

of diffusion orifices also required that the barium cermet insert be situated behind the filament surface where electrons are emitted. Coincidentally, due to spatial restrictions within the electron gun assembly and the set positions of the electrodes, Wehnelt focusing cup, and anode, this is the ideal location for a cermet. A predictive model using continuity and transport equations developed by Rubin and Williams was also adapted to the present work and validated against a prototype filament to guide the size and distribution of the holes used for the dispensing mechanism [31]. In Rubin and Williams, equations were developed that described barium diffusion from a cylindrically-shaped, impregnated tungsten insert to a single-orifice plate in a hollow cathode device. For the filament, similar equations were derived and utilized to describe barium migration through multiple orifices. An example of a plot generated from the modified model is shown in Figure 1.5.

The operation of the low work function filament is an amalgamation of the processes used for directly heated filaments and LWF cathodes discussed in Sections 1.2.1 and 1.2.2. Figure 1.8 shows a generalized schematic of a possible LWF filament configuration. The cermet insert, fashioned into a small disk, is enclosed within tantalum foil. A DC current between 30-40 A, about 20-30 A lower than the current needed to heat an unmodified filament, is flowed through the filament, which resistively heats it to the 1000-1200 °C, the temperature range necessary to create barium vapor from the insert. Barium vapor continuously condenses onto and re-evaporates from the interior filament surface and at the same time builds pressure within the enclosure. The barium adsorbed to the interior of the filament migrates via surface diffusion processes through the orifices in the emitter and begins to coat the exterior of the filament with a monolayer of barium atoms [31]. As barium atoms expand outward uniformly covering the surface, the barium coating

will reduce the work function of the tantalum substrate and enable the emission of electrons. While the process of barium production, migration, and surface diffusion continues, the LWF filament can maintain this reduced work function at relatively low heater currents for extended durations. Although barium is being sourced from the cermet, which could be considered a source of contamination in some applications, only very little barium is generated. Typically less than 1 mg is released over tens of hours of operation and a vast majority of this mass will condense on surfaces within the apparatus holding the filament rather than be released to a workpiece downstream.

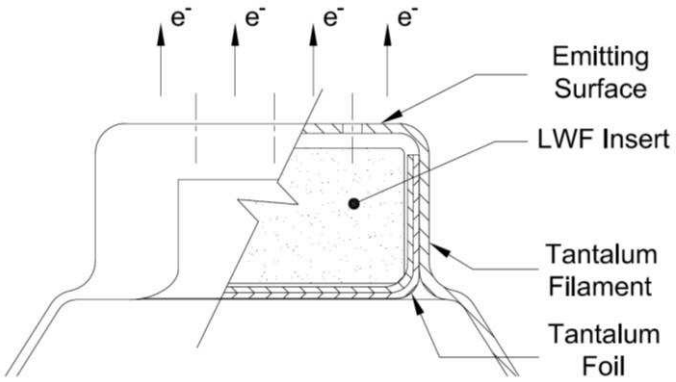

Figure 1.8: Cut-away of a LWF filament configuration. Centerlines indicate the location of barium diffusion orifices on the filament surface [27, 28].

Though the challenge of producing low work function inserts was largely solved through the collaboration with Plasma Controls, the work presented in this paper reports on the efforts to develop test procedures to evaluate LWF filaments and concurrently validate a computer model of barium diffusion to guide future designs. The necessity to include a controlled dispensing mechanism for barium is also investigated to determine the effect of excessive barium generation on arcing.

1.4 Thesis Outline

Chapter 2 discusses the parameters that were investigated in the various low work function filament configurations as well as the testing apparatus used to evaluate the filaments. Critical testing procedures, measurement techniques, and data analysis processes are also covered. Chapter 2 concludes with a discussion on the analytical model used to predict filament performance and reproduce empirically gathered data. The results from testing LWF filaments and analytical models are presented in Chapter 3. The issues and phenomena encountered during testing and the steps taken to address them are discussed as well. The thesis is concluded in Chapter 4 with a discussion of LWF filaments and their viability as a solution for EBAM filament lifetimes issues. Future work as it relates to further the development of a LWF filament is also presented in Chapter 4.

References

[1] Wohlers, Terry, Tim Caffrey, and Ian Campbell. Wohlers Report 2016 3D Printing and Additive Manufacturing State of the Industry. Fort Collins: Wohlers Associates, Inc., 2016.

[2] Taminger, Karen M.B., and Robert A. Hafley. "Electron beam freeform fabrication for cost effective near-net shape manufacturing." *NATO/RTO AVT-139 Specialists' Meeting on Cost Effective Manufacture via Net Shape Processing* (2006).

[3] Dave, V.R., J.E. Matz, and T.W. Eager. "Electron Beam Solid Freeform Fabrication of Metal Parts." *Proceedings of 6th SFF Symposium*, (1995): 64-71.

[4] Brice, C.A., D.S. Henn, D. Siedal, K. Lachenberg, and R. Salo. "Rapid Prototyping and Freeform Fabrication via Electron Beam Welding Deposition." *Proceeding of Welding Conference*, (2002).

[5] Gibson, I., D. Rosen, and B. Stucker. Additive Manufacturing Technologies: 3D Printing, Rapid Prototyping and Direct Digital Manufacturing. New York, NY: Springer, 2015.

[6] "Lockheed Martin Space Systems Advances Development of 3D-Printing for Critical Parts with EBAM." *Electron Beam Additive Manufacturing (EBAM).* Michigan Website Design, Sciaky, Inc. 2018. Web. 03 January 2018.

[7] Frazier, William E. "Metal Additive Manufacturing: A Review." *Journal of Materials Engineering and Performance* 23, no. 6 (2014): 1917-1928.

[8] *Sciaky User Manual: Section 6, Electron Beam Gun*, Sciaky, Inc., (1981).

[9] Cattelino, M.J., G.V. Miram, and W.R. Ayers. "A diagnostic technique for evaluation of cathode emission performance and defects in vehicle assembly." *Electron Devices Meeting, 1982 International*, (1982): 36-39.

[10] Miram, George, Lawrence Ives, Michael Read, Ross Wilcox, Mark Cattelino, and Brad Stockwell. "Emission Spread in Thermionic Cathodes." *Vacuum Electronics Conference, 2004. IVEC 2004. Fifth IEEE International*, (2004): 303-304.

[11] Langmuir, Irving. "The Effect of Space Charge and Residual Gases on Thermionic Currents in High Vacuum." *Physical Review* 2, no. 6 (1913): 450-486.

[12] Langmuir, Irving. "The Interaction of Electron and Positive Ion Space Charge in Cathode Sheaths." *Physical Review* 33, no. 6 (1929): 954-989.

[13] Goebel, Dan M., and Ira Katz. Fundamentals of Electric Propulsion: Ion and Hall Thrusters. Hoboken, NJ: Wiley, 2008.

[14] Windes, D., J. Dutkowski, R. Kaiser, and R. Justice. "Triservice/NASA cathode life test facility." *Applied Surface Science* 146, no. 1-4 (1999): 75-78.

[15] Justice, R., and A. Qualls. "TriService/NASA Cathode Life Test Facility 2002 Annual Report." Crane, IN: Crane Division, Naval Surface Warfare Center, 2002.

[16] Vancil, Bernard, Victor Schmidt, Ivor Brodie, Wayne Ohlinger, Jonathan Shaw, and Tyrus Monson. "Emission studies on reservoir cathodes. "*Vacuum Electronics Conference, 2008. IVEC 2008. IEEE International*, (2008): 165-166.

[17] Kaufman, Harold R., and Raymond S. Robinson. Operation of Broad-Beam Sources. Alexandria, VA: Commonwealth Scientific Corporation, 1987.

[18] Ehlers, K.W., and K.N. Leung. "Some characteristics of tungsten filaments operated as cathodes in a gas discharge." Review of Scientific Instruments 50, no. 3 (1979): 356-361.

[19] Jenkins, R.O. "A review of thermionic cathodes." *Vacuum* 19, no. 8 (1969): 353-359.

[20] Capece, Angela M., James E. Polk, and Joseph E. Shepherd. "Decoupling the Thermal and Plasma Effects on the Operation of a Xenon Hollow Cathode With Oxygen Poisoning Gas." *IEEE Transactions on Plasma Science* 43, no. 9 (2015): 3249-3255.

[21] Lipeles, R.A., and H.K.A. Kan. "Chemical stability of barium calcium aluminate dispenser cathode impregnants." *Application of Surface Science* 16, no. 1-2 (1983): 189-206.

[22] Cronin, J.L. "Modern dispenser cathodes." *IEE Proceedings I – Solid-State and Electron Devices* 128, no. 1 (1981): 19-32.

[23] Jacobson, D.L. and E.K. Storms. "Work Function Measurement of Lanthanum-Boron Compounds." *IEEE Transactions on Plasma Science* 6 no. 2 (1978): 191-199.

[24] Forman, R., and D.H. Smith. "Thermionic cathode life-test studies." *IEEE Transactions on Electron Devices* 26, no. 10 (1979): 1567-1572.

[25] Abrams, R.H, B. Levush, A.A. Mondelli, and R.K. Parker. "Vacuum electronics for the 21st century." *IEEE Microwave Magazine* 2, no. 3 (2001): 61-72.

[26] Ives, R. Lawrence, Louis R. Falce, Steve Schwartzkopf, and Ron Witherspoon. "Controlled Porosity Cathodes From Sintered Tungsten Wires." *IEEE Transactions on Electron Devices* 52, no. 12 (2005): 2800-2805.

[27] Farnell, Casey, Cody Farnell, John Williams, Desiree Williams, Bao Nguyen, Kathryn Greiner, and Ryan Ham. “Simplified Formation Process of a Low Work Function Insert.” US Patent Application No. Confidential. March 22, 2017.

[28] Nguyen, Bao, John Williams, Casey Farnell, Desiree Williams, Ryan Ham, and Kathryn Greiner. “Low Work Function Electron Beam Filament Assembly.” US Patent Application No. Confidential. May 20, 2017.

[29] Falce, L.R., and R.E. Thomas. “Controlled porosity dispenser cathode: Iridium-barium oxide.” *Electron Devices Meeting, 1978 International*, (1978): 156-159.

[30] Ives, R. Lawrence, Louis R. Falce, George Miram, and George Collins. “Controlled-Porosity Cathodes for High-Current-Density Applications.” *IEEE Transactions on Plasma Science* 38, no. 6 (2010): 1345-1352.

[31] Rubin, Binyamin, and John D. Williams. "Hollow cathode conditioning and discharge initiation." *Journal of Applied Physics* 104, no. 5 (2008): 053302.

2 Methods and Measurements

This chapter details the construction of the LWF filaments and the two testing apparatuses used to collect electron emission data from test articles: one in which the filament is immersed in plasma, and a second where it is operated as a vacuum emitter. Pre-test procedures, including system calibration and cermet conditioning, testing methodologies, and data analysis techniques are discussed next. This chapter concludes with the equations used to model the diffusion and desorption of barium and predict the resulting electron emission from a LWF filament.

2.1 Construction of LWF Filaments

Three components constitute the test articles examined: the cermet insert, the insert enclosure, and the tantalum filament. The following paragraphs discuss the details of how the cermet inserts were prepared and attached to filaments.

The simplified nature of forming cermets allowed flexibility in the composition of the insert. A handful of compositions that were tested early on were subsequently narrowed to a single composition that produced the most favorable emission. The cermet that became the basis for a majority of tests was composed of a 5:3:2 formulation of BaO-CaO-Al_2O_3 ceramic with trace amounts of scandate. A fine tungsten powder was used with the ceramic powder at a weight ratio of 5 (tungsten) to 1 (ceramic). All inserts were sintered in graphite crucibles in a furnace and had approximate diameters of .160” and thicknesses ranging from .050-.085”. Figure 2.1 shows a batch of inserts that had been faced on both sides in a lathe to a thickness of .050” after being sintered. Uneven shrinkage in the inserts, as shown in Figure 2.2, was observed in batches where ceramic and tungsten

mixtures were not adequately packed into the crucible prior to sintering, and, while this resulted in oblong-shaped cermet inserts, it is not believed to have affected their performance.

Removing the outer layer of an insert may eliminate possible surface-level blockages and expose more of the porous interior allowing barium vapor to more easily migrate out of the cermet. To study this the front-facing surfaces of inserts were prepared in three ways to determine the effect of post-sintering-surface-finish processes on emissive capabilities and determine a favorable balance between the current densities yielded and the time required to prepare inserts from a particular process. Figure 2.2 shows photographs of a selection of prepared inserts. A third of the inserts from a particular batch were left in their as-fired condition while another third were dry-polished using fine grit, alumina sandpaper. Contamination from sandpaper particles may not be of significant concern since alumina (Al_2O_3) is a constituent part of the ceramic. The remaining inserts were ion-beam polished for more than 20 hours at a glancing incident angle of ~84°. No additional inserts were prepared using the lathe as the laborious nature of the process and the low yield of inserts made this preparation option unfavorable. All inserts that were previously faced on a lathe were not included in tests described herein.

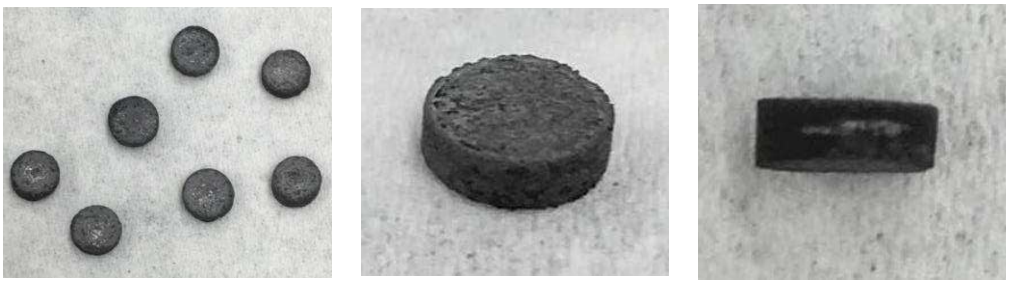

(a) (b) (c)

Figure 2.1: (a) The simplified formation process is capable of producing multiple inserts per batch. (b) and (c) provide close-up views of an insert that was faced on a lathe.

(a) (b) (c)

Figure 2.2: Low work function inserts: (a) as-fired, (b) dry-polished with sandpaper, and (c) ion-beam polished for 20+ hours.

Cermet inserts were enclosed within a basket made of two layers of .0005" thick tantalum foil that were formed using an aluminum die. The inserts and baskets were then carefully pressed into place behind the filament emitting surface as shown in Figure 2.3. The exposed portion of the foil around the outer diameter of the button filament was inspected with the Mantis Elite stereo microscope to ensure that the edge of the foil enclosure was tucked within the filleted outer edge of the planar, button surface. This enclosure served two purposes. When barium is released from the insert, the vapor will tend to condense onto nearby, relatively cooler surfaces such the electrodes holding the filament or on the upstream face and orifice barrel regions of the Wehnelt cathode. The basket enclosure and the seal it created with the button filament prevented the loss of barium to these and similar surfaces and also funneled the vapor to the filament surface. As radiation shielding, the foil helped to more effectively utilize the DC heating current by minimizing the radiative heat losses from the cermet.

All test articles used stock filaments from Sciaky made from .005" thick tantalum with emitter surfaces .175" in diameter and incorporated an array of holes to allow the dispensing of barium. These orifices were created using two methods. Figure 2.4(a) shows

a filament where a mill was used to drill an array of holes. The mechanical drilling produced burrs on the interior face of the filament and prevented inserts from seating properly. This operation also created surface blemishes and distortions that were difficult to repair. Figure 2.4(b) shows a filament with holes that were laser-burned using a laser-welder. The welder consisted of a small chamber, open to air but flooded with argon gas, where the workpiece was manually handled. The welding unit was capable of burning holes through the tantalum filament as small as .008" (.2 mm). Unfortunately the liquefied metal produced during exposure to the laser solidified into dross in the orifice of the drilled hole. This resulted in non-circular holes and dross that domed outward on the otherwise planar emitting surface of the filament.

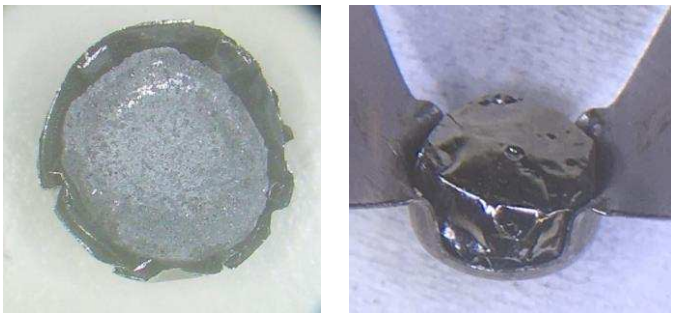

(a) (b)

Figure 2.3: The basket enclosure (a) around an insert and (b) assembled in a filament.

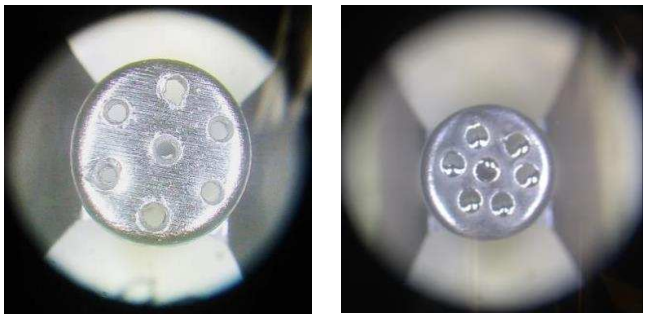

(a) (b)

Figure 2.4: Filaments with holes that were either (a) mechanically drilled or (b) laser-burned.

2.2 Test Configuration

An electron gun assembly consisting of a gun body, a porcelain insulating gun cap, a stainless steel cathode, a copper anode, and many .005" thick tantalum filaments were provided by Sciaky, Inc. The assembly was secured to an aluminum mounting plate on a stainless steel cart and installed within a 36" diameter vacuum chamber equipped with an Ion Tech GFC-1000-U gas flow controller, a TRIVAC D65BCS roughing pump, and an Osaka Vacuum TG3213EM turbo pump. The roughing pump was used to create initial soft vacuum conditions (10^{-2} Torr) while the turbo pump brought the chamber to hard vacuum operating conditions in the range of 10^{-6} to 10^{-7} Torr. The two testing configurations used for this research are described in the following sections.

Early tests were conducted in an apparatus that immersed the filament and portions of the electron gun assembly within a plasma, which reduced space charge and allowed the current of thermionically emitted electrons from the filament to be measured. Plasma was generated by an instant-start, heater-less hollow cathode nested within a discharge anode shroud. Figure 2.5 shows the plasma source and electron gun as it was installed in the chamber. The plasma source was mounted on a swivel and manually rotated in-line with the electron gun during operation and then rotated "out of the way" to allow measurement of the brightness temperature of the filament. Figure 2.6 provides general and electrical schematics of the plasma-immersed configuration.

During operation a gas flow controller was used to set a flow rate of 30 sccm of argon gas to the hollow cathode. The cathode was electrically connected to ground. A Sorensen XG 600-1.4 power supply was used to positively-bias the keeper relative to the cathode to initiate an arc discharge. The keeper potential dropped to less than 10 V after

the plasma was established and stabilized. A Sorensen DCS 150-7 was used to bias the anode shroud positive of the cathode to draw 7 A of discharge current. The anode voltage was ~32 V +/- 2 V. The discharge created downstream of the cathode by the electrons immersed the filament in a dense plasma. Discharge plasma immersion of the filament was only performed when extracting electrons from the test article. The filament temperature was set with a Sorensen DCS40-75E using currents up to 60 A. The filament supply was floated above a bi-polar Kepco BOP 50-4M that biased the filament -10 V relative to ground. The Wehnelt cylinder was biased -21 V to ground using a TDK-Lambda ZUP20-10 power supply. Voltages for the discharge anode, filament heater, and filament bias were recorded using multimeters. The voltage across a 1 Ω resistor wired upstream of the filament bias power supply was used to measure the current flowing from the filament to the plasma. The electron emission current was determined from the measured current by subtracting the ion current flowing from the plasma to the filament, which was measured when the filament was cold.

(a) (b)

Figure 2.5: The high density plasma source located on the right side (a) as it appears when it is rotated away from the filament to allow brightness temperature measurements, and (b) facing the electron gun during electron emission testing.

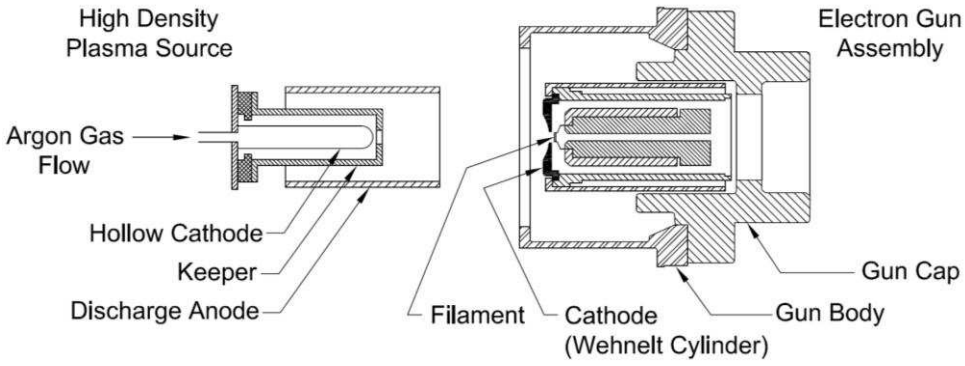

(a)

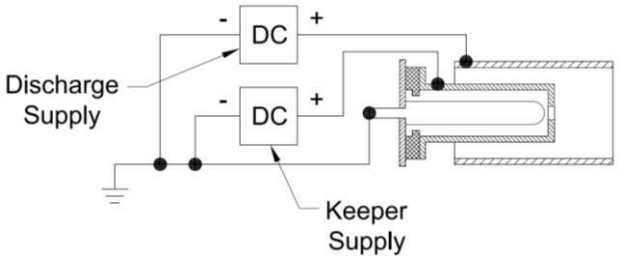

(b)

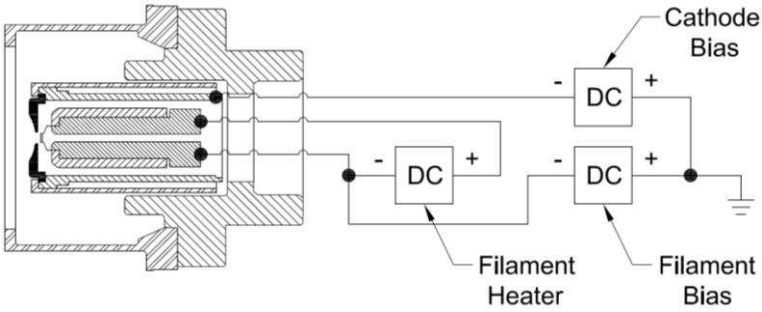

(c)

Figure 2.6: A schematic of the plasma generator and electron gun assembly is shown in (a) and their respective electrical schematics are shown in (b) and (c).

Following these early tests of the filament, the testing apparatus transitioned from the plasma-immersed set up to one performed in a vacuum environment. This allowed for the filament's performance to be measured in operating conditions that more closely mimicked a production EBF^3/EBAM unit. The use of the vacuum configuration eliminated plasma ion bombardment of the filament that could potentially modify its surface.

A majority of the tests conducted for this research were performed in the vacuum emission configuration that operated in the absence of the plasma generator. In place of it, electron emission was collected on a water-cooled, aperture anode assembly. Figure 2.7 illustrates the arrangement of the electron gun and anode assembly and their respective electrical connections while Figure 2.8 shows a photograph of the apparatus as it appears in the vacuum chamber. The anode assembly was mounted directly to and grounded through the electron gun body and designed so that anodes mounted to the support block could be positioned between .020-.060" from the filament. The power supply providing the negative bias to the cathode Wehnelt cylinder relative to the filament was also removed from the system following early tests where frequent arcing events were observed between the filament and cathode. The arcing was problematic for data acquisition, and furthermore the cathode's function as a focusing element and an emission suppressor were not required for testing.

A Universal Voltronics BRC 10000 (3000 V, 3.333 A) power supply capable of providing a high voltage, negative bias to the filament replaced the Kepco BOP 50-4M bi-polar power supply used in the plasma-immersed configuration. A 500 Ω inline ballast resistor and a 2000 Ω load resistor placed across the BRC 10000 terminals were used with the BRC 10000 to stabilize the supply output and protect the filament being tested from being damaged by a high current arc. A TDK-Lambda GEN8-180, used for heating the filament, was floated at high voltage and as such, required safety measures to protect lab personnel. All power supplies were installed in a cabinet, as shown in Figure 2.9, and the filament heater was shielded with acrylic and powered through an isolation transformer.

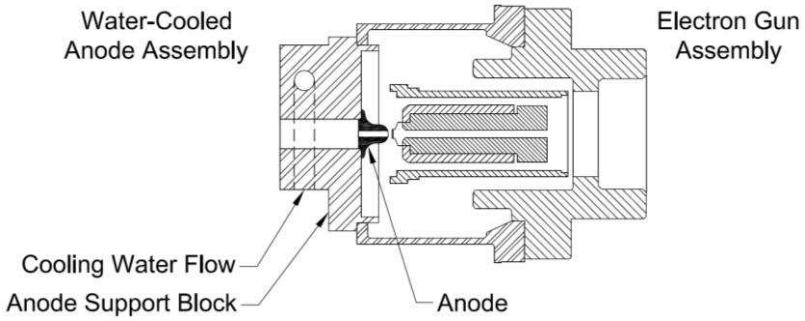

(a)

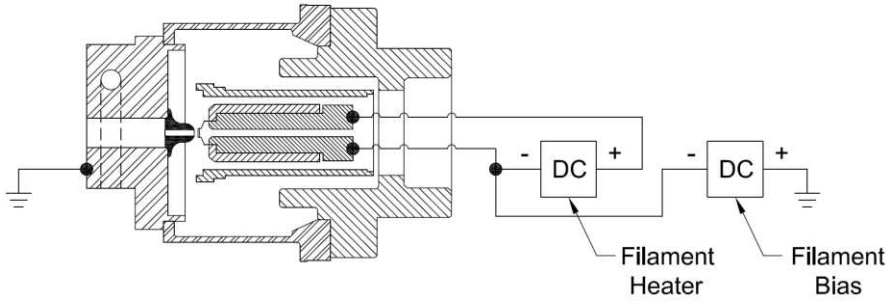

(b)

Figure 2.7: Schematic of the water-cooled anode and electron gun assembly is shown in (a), and its electrical schematic is shown in (b).

(a)

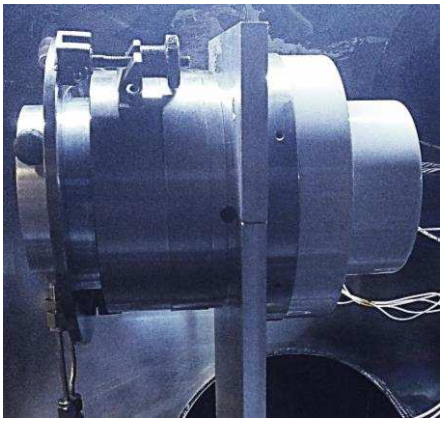

(b)

Figure 2.8: Vacuum emission testing configurations with the (a) anode assembly separated from the electron gun, and (b) fully assembled with a steel retaining ring securing the anode assembly to the gun body.

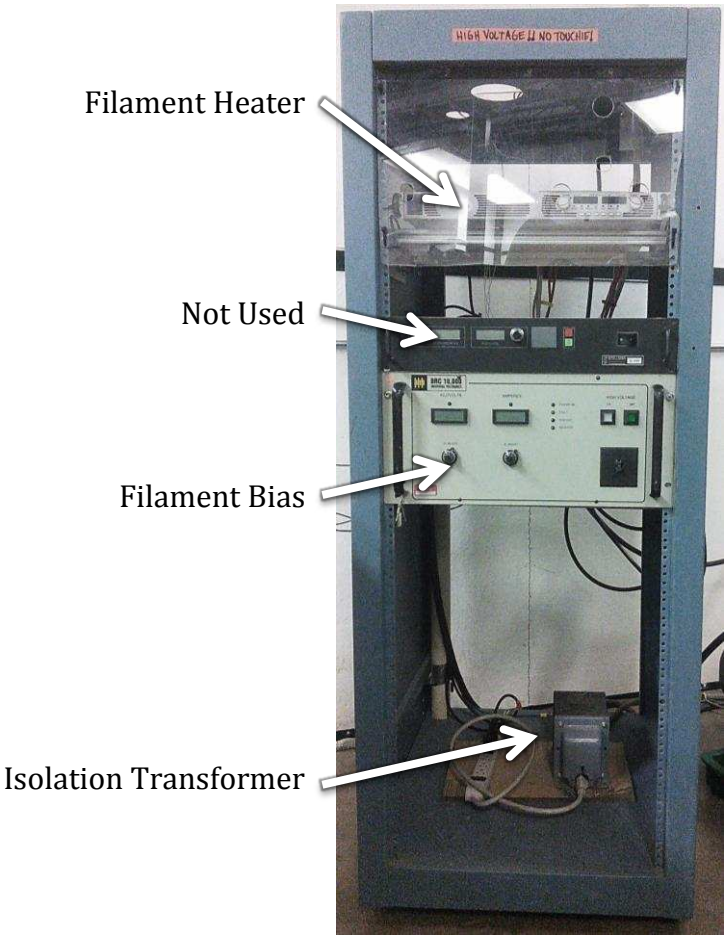

Figure 2.9: Power supply cabinet used with the vacuum emission testing configuration.

Close spacing between the filament and anode and accelerating voltages up to 3 kV helped to create testing conditions that were not severely space-charge limited. To determine the actual current from the filament, electrons had to be collected by the anode, but continued bombardment with high energy electrons would quickly heat the anode and potentially cause it to sublimate. This could lead to contamination of the filament surface, encourage the initiation of arcs, or alter the space-charge effects on the emitter. Heat input was, therefore, managed by water-cooling the aluminum support block holding the anode and through pulsing the high voltage applied to the filament [1, 2, 3, 4]. The bias from the high voltage power supply was electronically controlled through a National Instruments

USB-6002 Multifunction I/O unit coupled with a simple LabVIEW VI. The VI contained waveform generators that created sine waves, limited to single-valued voltages, and square and ramped waveforms that were capable of applying three different biases with independently controlled durations. The latter created a convenient and efficient method for evaluating three loading conditions for a filament at a given heating current. Pulse durations ranged from between 250 milliseconds to 1 second depending on the voltage applied. The USB-6002 was also used as a data acquisition unit to collect system currents that were later processed to determine the electron emission. All cables used with the USB-6002 were shielded to reduce noise and interference from the laboratory testing environment.

2.3 Procedures

Several steps were required to prepare for testing and included setting bias parameters, calibrating the system, and conditioning the cermet. Tests consisted of recording emission currents, evaluating the repeatability of emissions following multiple air exposures, and maintaining emissions during extended run-time tests.

Stock tantalum filaments are installed into production electron guns using an insertion tool that ensures a gap distance of .575” is consistently established between new filaments and the anode. The same tool was used to install LWF filaments into the gun assembly at smaller gap distances of .020-.060”; however, the presence of the cermet causes variations in the axial position of the filament within the gun assembly. As a result with each installation of a test article, the filament-to-anode gap was measured with a digital depth micrometer and verified to be between .020-.060”. The emission current

measurements were typically made using ramp waveforms to maximum applied voltages of 500 V, 1000 V, and 3000 V.

After pumping down the chamber to pressures between 5 x 10^{-6} Torr and 8 x 10^{-7} Torr, the system was calibrated to the particular test article by characterizing the system's electrical resistance with no heating current. An applied voltage was plotted against the resulting current yielding the reciprocal of the system's resistance. The slope and intercept produced from a simple linear regression fit of the data were extracted and used to process current data collected by the DAQ unit during an actual test to determine the emission current of the LWF filament.

With each exposure to air, contaminants, such as water vapor, carbon dioxide, and oxygen, can infiltrate the cermet insert and adsorb in and on the material. If traditional barium-tungsten inserts are heated too quickly, the contaminants can cause irreversible chemical reactions to occur, poisoning the insert, and negatively affecting the cathode's performance [4]. Poisoning can also occur if an insert is exposed to air before it is allowed to sufficiently cooldown. This would subsequently require operating the filament at a higher temperature to maintain the minimum emission current resulting in accelerated barium evaporation and reduced usable lifetime [5]. It is possible that the cermet material is more robust than traditional inserts, but demonstration of this is beyond the scope of this thesis. Consequently possible cermet poisoning can be avoided through a conditioning process that safely removes these contaminants. This was done once the filament was at hard vacuum and involves slowly heating the filament and cermet to allow the outgassing of contaminants [4]. Conditioning can take from minutes to hours depending on the cathode, the type of contaminant, the amount of exposure, the temperature during

exposure, and the reactivation temperature [6]. Since common materials were used in both, the conditioning procedure outlined by Rubin and Williams [4] for a hollow cathode was used to guide the conditioning procedures for the cermet-equipped filaments. Table 2.1 lists the conditioning sequences used, which specifies the heater current and the duration at which the filament was held.

Table 2.1: LWF Filament conditioning sequence.

Heater Current (A)	Sequence #1 (min)	Sequence #2 (min)
10	3	5
20	3	5
30	3	5
40	3	5

When tested, a heating current of a specified amperage was applied to the LWF filament. Adequate time was allowed to elapse to reach steady state before a brightness temperature measurement of the test article was made using a disappearing filament pyrometer. The pulse bias waveform was then applied to the filament via the USB-6002 unit, which was also used to acquire the gross system current collected by the anode. This general procedure was used with heating currents between 30-40 A (with incremental changes of 1 A) to produce electron emission data over a range of operating temperatures. Certain test articles were then exposed to air and then re-tested using the same procedure. Prior to exposing the filament to air, test articles were allowed to cooldown in vacuum for thirty minutes to avoid poisoning the cermet. Air exposure tests were repeated up to two times. Other test articles would be run with a modified procedure for at least 50 hours without exposure to air to determine if the LWF filament could appreciably extend the run-time allowance of EBF^3/EBAM units. Filaments in these tests were set to a heating current

to establish a 200 mA minimum electron emission current. The heating current was adjusted over the course of 50+ hours as necessary to maintain 200 mA emission until heating currents exceeded 40 A.

The disappearing filament, optical pyrometer that was used to measure brightness temperatures was made from a .010" diameter, tantalum wire and situated within the vacuum chamber between the electron gun assembly and chamber view window. The brightness of the test article, which was visible through the aperture in the anode, was matched with the wire that was made to be incandescent using currents up to 6 A. A previously developed thermal model was used to determine the brightness temperature of the test article based on the wire's current. Temperatures of test articles varied at a given heating current, but it was observed that, on average, currents from 30-40 A were roughly equivalent to brightness temperatures between 900-1275°C. All temperatures reported in this research and associated with experimental data are implied to be brightness temperatures. Aperture anodes were present only in the vacuum emission configuration. In the plasma-immersed configuration, it was necessary to rotate the plasma generator away from the electron gun to make temperature measurements. This can be seen in Figure 2.10.

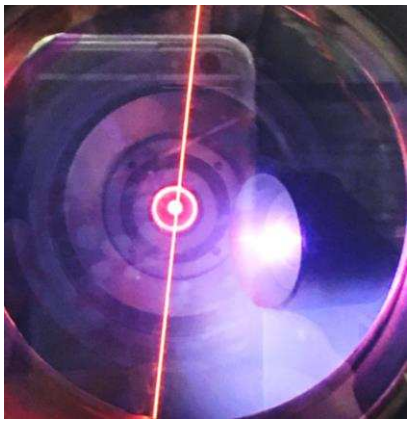

Figure 2.10: The disappearing filament wire runs vertically across the view window and appears directly in front of the test article positioned at the center of the gun.

2.4 Data Processing

The voltages and currents collected by the USB-6002 were run through a MATLAB script, which is included in Appendix C. It was written to expedite the processing and plotting of raw data. Thermionic electron emissions and their associated voltages were extracted using the slope, *m*, and intercept, *b*, from the calibration curve and Equations 2.1 and 2.2. J_{raw} and V_{raw} are the system current in mA and applied voltage in V returned by the DAQ unit, and J_T and V_T are the true electron emission in mA and voltage in V at the filament. *R* is the value of the ballast resistor in ohms used with the BRC 10000 power supply.

$$J_T = J_{raw} - (m * V_{raw} + b) \tag{2.1}$$

$$V_T = V_{raw} - \left(\frac{J_T}{1000}\right) * R \tag{2.2}$$

The resulting data set was further processed through a simple digital filter that generated plots similar to the one shown in Figure 2.11, which indicates true voltages - V_1, V_2, V_3 - and true emission – J_1, J_2, J_3 – at a specific temperature. The applied bias, in this case, used a 3-step ramped waveform with a short dwell between ramps. The emission currents are collected and compared to the predicted emissions from a plot similar to Figure 1.5 that was calculated for a filament at the same temperature.

The processed data was also used to calculate the effective work function of the test article with the help of Schottky plots. Figure 2.12 is an example of such a plot, which was used to validate the vacuum emission configuration for measuring work functions using a pure tantalum filament (~4.2 eV). At a constant filament temperature, the natural log of the emission current was plotted against the square root of the voltage that produced a curve

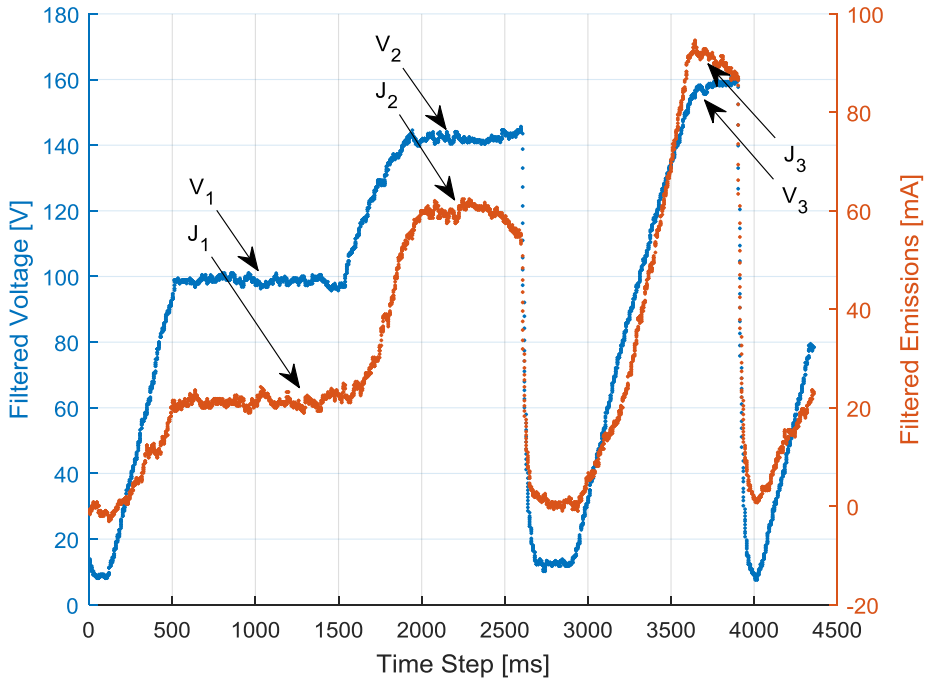

Figure 2.11: Voltages (blue) and emissions (orange) from a LWF filament tested at 40 A.

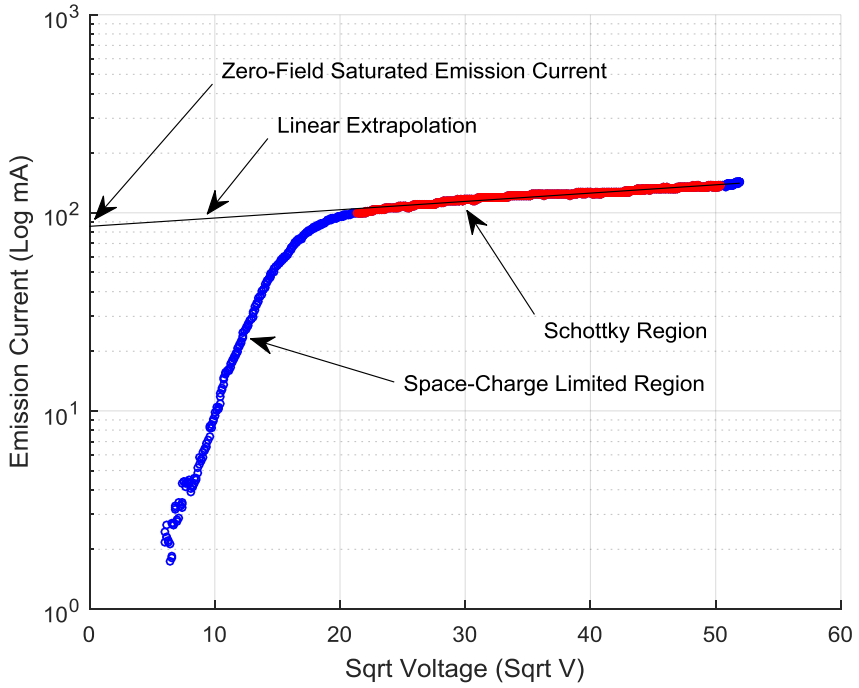

Figure 2.12: A Schottky plot obtained from an unmodified, tantalum filament.

featuring a prominent knee followed by a positively-sloped linear section referred to as the Schottky region. This region begins at a voltage in which a saturation current for thermionically emitted electrons is reached and characterized by the extraction of additional emissions through an increasing applied electric field that slightly reduces the work function [7]. The increased emission current in this region is accounted for by the Schottky effect included in the field enhanced Richardson-Dushman equation. A linear extrapolation of the Schottky region to the point where the voltage and surface electric field are zero yields a value known as the zero-field saturated emission current. This value, along with the filament temperature and Equation 1.2, is used to back-calculate the work function of the test article. Note that MATLAB does not have the functionality to create plots with a natural log scaled axis, so Schottky plots generated in this research, including Figure 2.12, use a log base-10 axis scale for visual aesthetics. MATLAB script calculations, however, for the zero-field emission current are properly made using the natural logarithm.

2.5 Analytical Modeling

The MATLAB emission model developed in this thesis was adapted from an existing model by Rubin and Williams [4] for a hollow cathode consisting of a barium calcium aluminate insert placed behind a tungsten orifice plate. Three equations represented the core of the existing model and remained at the foundation of the code developed here to describe LWF filaments.

2.5.1 Transient Surface Diffusion and Emission Model for Hollow Cathodes

The model by Rubin and Williams began with the continuity equation shown in Equation 2.3 which describes the time rate of change in the fractional surface coverage of barium vapor adsorbing to and diffusing from the inner surface and orifice barrel of the hollow cathode. The fractional surface coverage, θ_0, of barium on the inner surface and orifice barrel was limited to a monolayer due to the rapid, bulk evaporation of any additional layers [8]. The remaining terms - k_a, a term associated with the adsorption of barium and proportional to its partial pressure within the cathode and τ, the desorption time for a barium atom - were dependent on the cathode's temperature and derived from empirically determined values. The adsorption and desorption terms were set equal to each other to determine the fractional surface coverage at a given temperature for steady-state conditions.

$$\frac{\partial \theta_0}{\partial t} = k_a(1 - \theta_0) - \frac{\theta_0^5}{\tau} \tag{2.3}$$

A second equation similarly described the change in fractional surface coverage but on the exterior face of the orifice plate due to barium diffusion from the orifice barrel and its desorption from the surface. This behavior is defined in Equation 2.4 where θ is the fractional surface coverage and D is a temperature dependent, surface diffusion coefficient. The partial differential equation was simplified to one-dimension in space, since barium diffusion was limited to a single monolayer, with boundary conditions based on steady-state values of θ_0 at the orifice edge and at a radius sufficiently far from the orifice plate's outer edge.

$$\frac{\partial \theta}{\partial t} = D\nabla^2\theta - \frac{\theta^5}{\tau} \tag{2.4}$$

The reduced work function due to $Ba^{+}O^{-}$ dipoles was determined through a relationship derived by Longo et al. [9] shown in Equation 2.5. The overall work function, ϕ measured in eV, of the orifice plate was solved as a function of the barium fractional surface coverage and was also dependent on ϕ_W, the work function of tungsten in eV, ϕ_{Ba}, the work function of barium in eV, and Γ, a non-dimensional parameter derived by Longo for determining the work function for monolayer coverage.

$$\phi(\theta) = \phi_W \left(\frac{\Gamma\phi_W}{\phi_{Ba}}\right)^{\Gamma\theta/(1-\Gamma)} + \phi_{Ba}\left[1 - \left(\frac{\Gamma\phi_W}{\phi_{Ba}}\right)^{\theta/(1-\Gamma)}\right] \tag{2.5}$$

The resulting overall work function was then used in Equation 1.2 in conjunction with the cathode temperature, in Kelvin, and electric field strength, in V/m, between the cathode and keeper to determine the TL current density. This current density was integrated over the area of the orifice plate to solve for the thermionic emission current from the hollow cathode.

2.5.2 Transient Surface Diffusion and Emission Model for LWF Filaments

The Rubin and Williams model was extended to include an evaluation of emission currents over a range of temperatures with a set number of equally spaced holes in the TL, SCL, and SCL-TL knee regions. The new emission model was divided into two MATLAB scripts: a parent code that allowed testing parameters to be set, and a child code that evaluated TL emissions using the parameters as input arguments.

Parameters, such as the temperature range, hole quantity and size, applied voltage, and filament-to-anode gap, were specified in the parent code and iteratively passed to the

child code to solve for the TL emission and work function at each value specified in the temperature range. The parent code also solved for the SCL emission using the loading condition and emitting surface area of the filament. Equation 2.6, originally suggested by Longo [10], was used to model the emission densities in the SCL-TL transition region. The shape factor, α, accounts for the surface coverage uniformity of barium over the emitter and was originally used by Longo to model the effect of barium depletion due to cathode ageing on electron emission. Longo reported that, early in life, traditional dispenser cathodes would have shape factors of 3.5, corresponding to sharp, pronounced knees in the transition region, that decrease to values close to 1 over the course of 60,000 hours. The application of the shape factor in this research was used to provide insight into the effect of filament design (hole quantity, diameter, and placement) and cermet barium production rates that can be affected by air exposure or due to conditioning/activation transients at initial operation.

$$\frac{1}{{j_{TOT}}^{\alpha}} = \frac{1}{{j_{TL}}^{\alpha}} + \frac{1}{{j_{SCL}}^{\alpha}} \tag{2.6}$$

The child code incorporated the existing model and empirical constants developed by Rubin and Williams and also determined the distribution of emissions per hole for a test article with an array of orifices. The work function of the substrate material in Equation 2.5, however, was updated to represent the tantalum filament instead of the tungsten orifice plate. The simple distribution of emissions was determined by evenly dividing the emitting area of the filament among the specified number of holes which created several pseudo-physical boundaries. This is shown in Figure 2.13. The emission density for one of these subdivisions was solved using an extended boundary as the outer boundary

condition for Equation 2.4. Emissions associated with the annulus between the pseudo-physical and extended boundaries were subtracted, and the remainder was multiplied by the number of holes to produce a close estimation of the total TL emission from the LWF filament. The cross-hatched areas indicated in the multi-orifice model are unaccounted for in this simplified emission distribution, which means the estimation skews to a worst-case, underestimated condition. Both the TL emission current and the calculated work function were returned to the parent code as single-valued results.

An example plot generated from this code is shown in Figure 1.5. Code for the emission model is included in Appendix C, and because of its parent-child coding structure, the model can be easily expanded to evaluate emissions over a range of voltages, holes sizes, and quantity of holes as well.

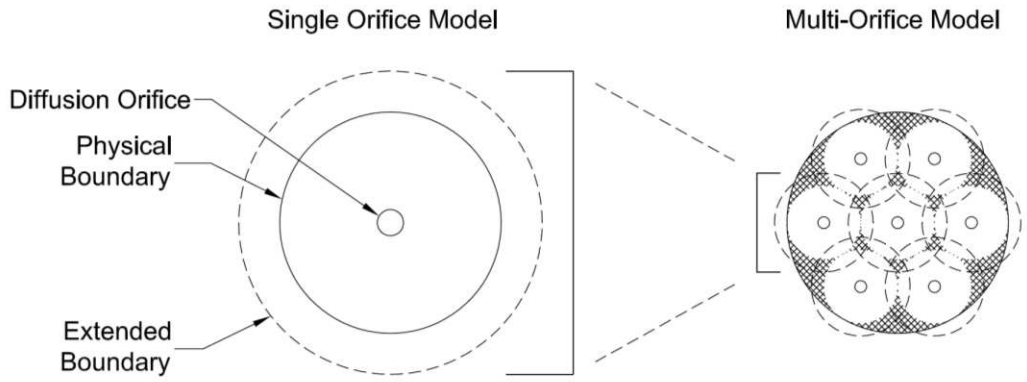

Figure 2.13: A diagram illustrating the simple distribution method used to determine electron emission from each diffusion orifice in the emitter.

References

[1] Wright, D.A. “Thermionic Emission from Oxide Coated Cathodes.” *Proceedings of the Physical Society, Section B* 62, no. 3 (1949): 188-203.

[2] Rittner, E.S., R.H. Ahlert, and W.C. Rutledge. “Studies on the Mechanism of Operation of the L Cathode. I.” *Journal of Applied Physics* 28, no. 2 (1957): 156-166.

[3] Windes, D., J. Dutkowski, R. Kaiser, and R. Justice. “Triservice/NASA cathode life test facility.” *Applied Surface Science* 146, no. 1-4 (1999): 75-78.

[4] Rubin, Binyamin, and John D. Williams. "Hollow cathode conditioning and discharge initiation." *Journal of Applied Physics* 104, no. 5 (2008): 053302.

[5] Capece, Angela M., James E. Polk, and Joseph E. Shepherd. "Decoupling the Thermal and Plasma Effects on the Operation of a Xenon Hollow Cathode With Oxygen Poisoning Gas." *IEEE Transactions on Plasma Science* 43, no. 9 (2015): 3249-3255.

[6] Marrian, C.R.K., G.A. Haas, A. Shih. “Fast turn-on characteristics of tungsten-based dispenser cathodes following gas exposures.” *Applications of Surface Science* 16, no. 1-2 (1983): 73-92.

[7] Burtner, D, and P.J. Wilbur. “Plasma Contacting with a Solid Expellant.” *37th AIAA Aerospace Sciences Meeting and Exhibit*, (1999): 99-0381.

[8] Jensen, K.L., Y.Y. Lau, and B. Levush. “Migration and escape of barium atoms in a thermionic cathode.” *IEEE Transactions on Plasma Science* 28, no. 3 (2000): 772-781.

[9] Longo, R.T., E.A. Adler, and L.R. Falce. “Dispenser cathode life prediction model.” *Electron Devices Meeting, 1984 International*, (1984): 318-321.

[10] Longo, R.T. “Physics of Thermionic Dispenser Cathode Aging.” *Journal of Applied Physics* 94, no. 10 (2003): 6966-6975.

3 Results and Discussion

Chapter 3 presents the results of this research and begins by addressing the specific aims established earlier in this thesis in extending the runtime of filaments. This chapter continues with an examination of the work functions obtained from testing as well as observations on the effect of filament construction on measured emission currents. The validation of an analytical model developed as a tool to predict the emission of filament designs follows, and the chapter is concluded with a short discussion on the phenomena observed during the research project.

3.1 Extended Runtime Results

The amount of barium ceramic present within a low work function insert and its operating temperature, which affects the rate of barium evaporation, are two of the primary life-limiting factors for a dispenser cathode. If the barium ceramic in an insert is exhausted or the gas-tight seal between the cathode and the emitter surface is compromised, barium vapor can no longer be produced or directed to where it is needed, which eliminates the work function reducing mechanism in the cathode. The difference in barium rich and partially-depleted cermets is shown in the SEM images in Figure 3.1. Both cermets were ion-beam polished prior to imaging. An un-tested cermet with distinctive regions of barium ceramic and tungsten can be identified in Figure 3.1(a). Figure 3.1(b) shows an insert tested for 12 hours to temperatures up to 1443°C in the vacuum emission configuration. Surface-level barium ceramic is notably absent, having been decomposed and evacuated during testing, and reveals the underlying porous tungsten matrix. Although barium ceramic on the surface is depleted, additional barium vapor can be sourced from

ceramic located in the interior structure of the tungsten matrix until its supply is completely exhausted.

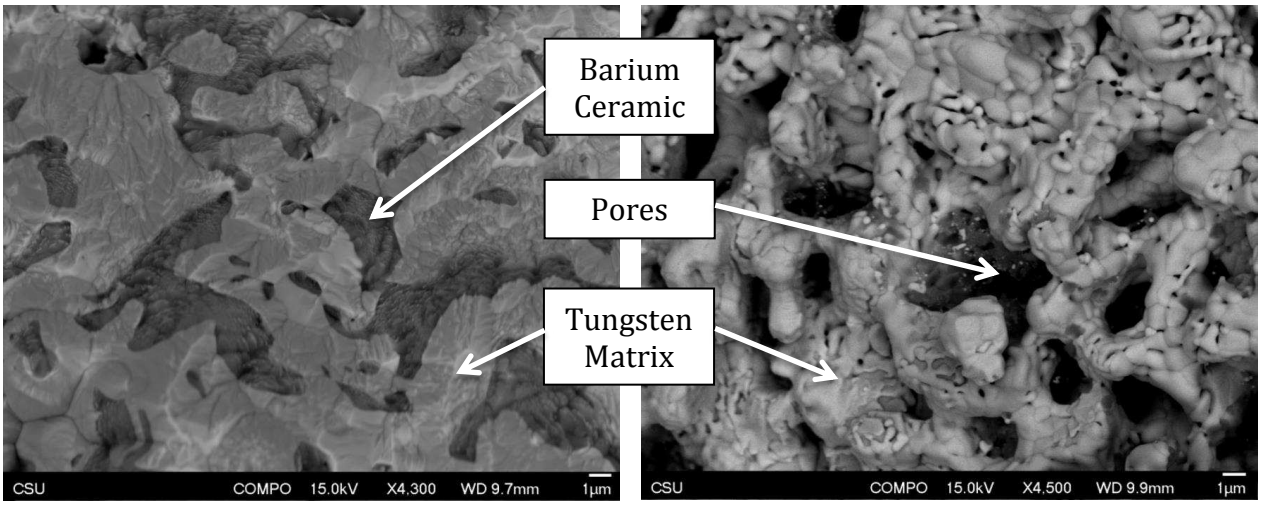

(a) (b)

Figure 3.1: SEM imaging of (a) un-tested and (b) tested ion-beam polished cermets sintered in air. The tested cermet was run for over 12 hours.

An extended runtime test used to investigate the LWF filament's ability to maintain an emission current consistent with the nominal operating point of EBAM systems was conducted over a 75 hour period in the plasma-immersed chamber configuration. The primary molar composition (5:3:2) and tungsten-to-ceramic weight ratio (5:1) of the cermet tested was consistent with those used throughout this research, and the test piece was measured to be .050" thick with a diameter of .160". The heating current was set to a value between 30 A (~900-950°C) and 40 A (~1200–1225°C) that would produce the 200 mA minimum emission current. It was left at that setting until the electron emission would begin to deviate at which point the heating current would be increased or decreased accordingly. The plasma ion current to the filament was 6 mA, and it remained constant from the start of the test and up to its conclusion. Discharge currents to the anode were applied in a pulsed fashion by quickly ramping up to the 7 A maximum and back down to 0

A. Peak emission currents were measured from a multimeter. The plasma generator was left in keeper mode when electron emission was not being measured to avoid contaminating the test article from repeated cathode start-ups.

Figure 3.2 summarizes the runtime test and indicates the emission threshold for EBAM units with a solid black line. Gaps in data before and after the second testing block represent recesses in which the vacuum chamber was left unattended. Initial adjustments to the heater current were required to establish a steady 200 mA emission current in the first 2 hours of the runtime test but required relatively less adjustment for the remainder of the first testing block, which maintained the 200 mA emission with heating currents between 31–32.5 A. The decrease in electron emission in the second testing block was likely due to a drop in the test article's temperature. During the first testing block, the plasma source remained in front of the test article and likely accounted for a portion of the heating to the filament, despite running in keeper mode, allowing the filament heater current to remain at a relatively low amperage. However at the start of the first testing recess, the plasma source was rotated away from the filament allowing the test article to equilibrate to a lower temperature consistent with the applied heating current. The cermet also benefitted from the conditioning procedure that preceded the start of the first testing block. Data in the final testing block were characterized by fluctuations in emission current possibly due to uneven or restricted sourcing of barium vapor from the interior of the cermet [1]. The observed average emission (~300 mA) is also greater than previous testing blocks and occurs at lower heating currents indicating that the cermet may have reached a partial or fully activated operating condition resulting in an elevated emission output. Proper activation of impregnated cathodes, which is different from the outgassing of

contaminants during conditioning, can result in increased emission and may take on the order of hundreds of hours, but full activation has also been observed to occur in times as low as 3 hours (depending on activation temperature) [2].

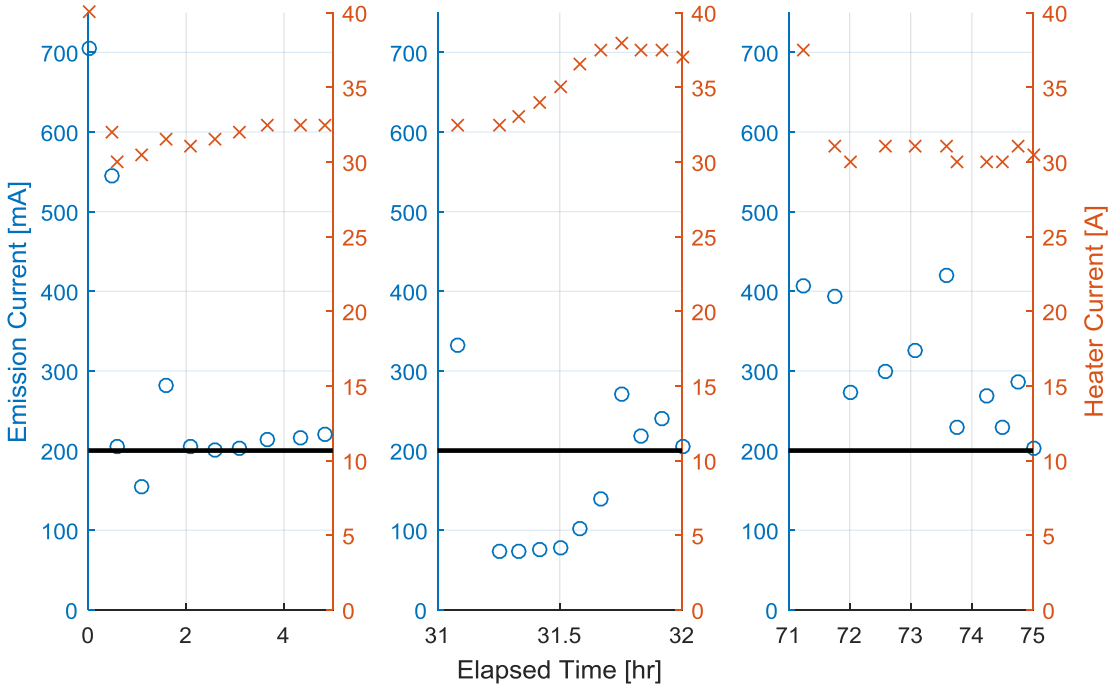

Figure 3.2: Plasma electron emission ('o') and heater current ('x') over a 75 hour extended runtime test with the emission threshold indicated by the bold line.

A subsequent test using a test article (with a similarly sized emitter surface area and a cermet insert .072" thick) as a vacuum emitter examined emission currents collected at 1000 V over 8.5 hours of testing. The nature of the test was intended to determine the agreement between collected emission currents to the TL emission model as well as emission behavior in DC bias conditions. But it concurrently provided insight into the extended runtime performance of the filament in testing conditions absent of plasma. Figure 3.3 presents the data collected as a function of the brightness temperature, which were obtained using heating currents between 35-40 A. The emission currents increased

over the course of the test period due to partial activation of the cermet but are less than the target 200 mA emission current, reaching as high as 151 mA. These comparatively lower emission currents are caused by space-charge effects which will be less pronounced in EBAM systems operating with accelerating potentials of 40 kV. EBAM systems will also see ~32% greater electron emission currents due to Schottky enhancement effects.

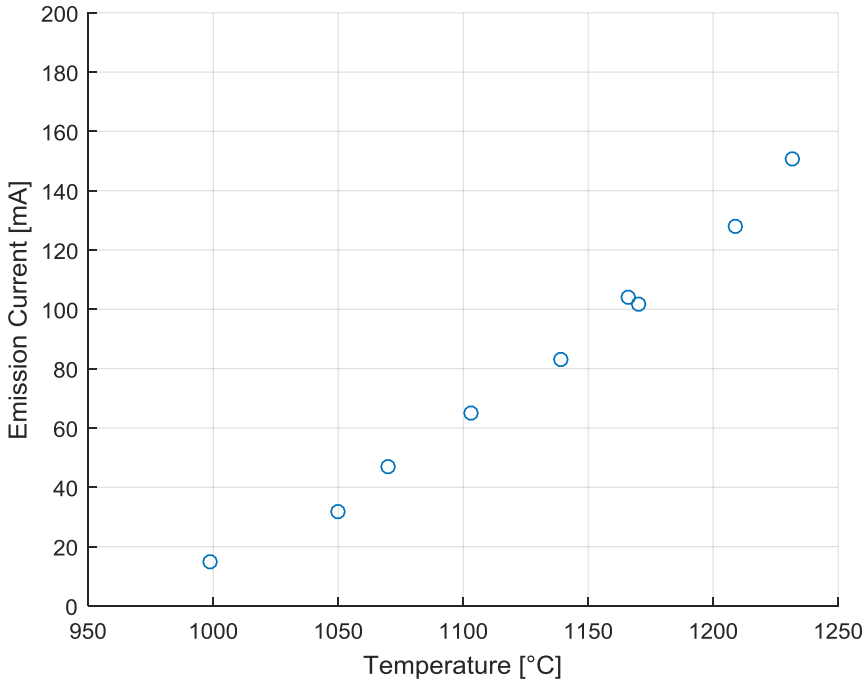

Figure 3.3: Vacuum electron emission measured at the end of an 8.5 hour test at 1000 V.

Although the use of plasma effectively increased the electron emission from the test article, which otherwise would have been highly space-charge limited [3], this does not diminish the data collected from the extended vacuum runtime test. The electron emission currents observed throughout the test indicated the continuous production of barium vapor over 75 hours and demonstrated that the barium ceramic available within the cermet was sufficient for extended runtimes. The following vacuum emission test revealed

that (1) increased electron emission could be observed without the aid of plasma interactions and (2) a LWF filament could be operated for more than twice the nominal lifetime of an unmodified tantalum filament. Finally, it is pointed out that both tests were voluntarily terminated and not because of a failure.

3.2 Comparison of LWF Filament Formation

Work functions for each test article were calculated using the Schottky method discussed earlier and were compared to published values obtained for similar low work function, impregnated inserts. Recall that the Schottky plot methodology as well as the testing apparatus and the MATLAB scripts used to collect data and calculate an emitter's work function were validated by testing an unmodified, tantalum filament at the highest ramp voltages. The average work function was found to be 4.22 eV with a standard deviation of .04 eV and provided an acceptable level of accuracy with published values for tantalum. The emission currents reported here and throughout the remainder of this chapter were collected using the filaments as vacuum emitters – i.e. plasma was not present during these tests.

The average work functions for LWF filaments obtained over temperature ranges between 1000 and 1250°C are shown in Figure 3.4 for three different peak ramp voltages. The cermet tested at 500 V had an ion-beam polished surface and was conditioned using sequence #2 shown in Table 2.1. Both cermets tested at 1000 V and 3000 V had as-fired surface finishes and were conditioned with sequence #2 and #1, respectively. Work functions as low as 2.47 eV and 2.63 eV were calculated near 1000°C at 1000 V and 500 V, respectively, and a 2.37 eV work function was calculated at 1070°C at 3000 V. It is expected to see a relatively consistent work function over the range of temperatures, but calculated

values increased as the test article's temperature was elevated. This is likely due to a non-uniformity or low fractional surface coverage of $Ba^{+}O^{-}$ dipoles which can result from localized areas of cathode poisoning on the emitter's surface or the temperature-dependent, evaporation rate of barium [4]. Cathode poisoning can prevent the formation of dipoles and accelerated evaporation rates can shorten the length of time barium is allowed to remain on an emitter's surface. Ultimately, both mechanisms can increase the emitter's effective work function. The calculated work functions, therefore, also indicate that $Ba^{+}O^{-}$ dipoles are at their greatest coverage between 1000°C and 1100°C.

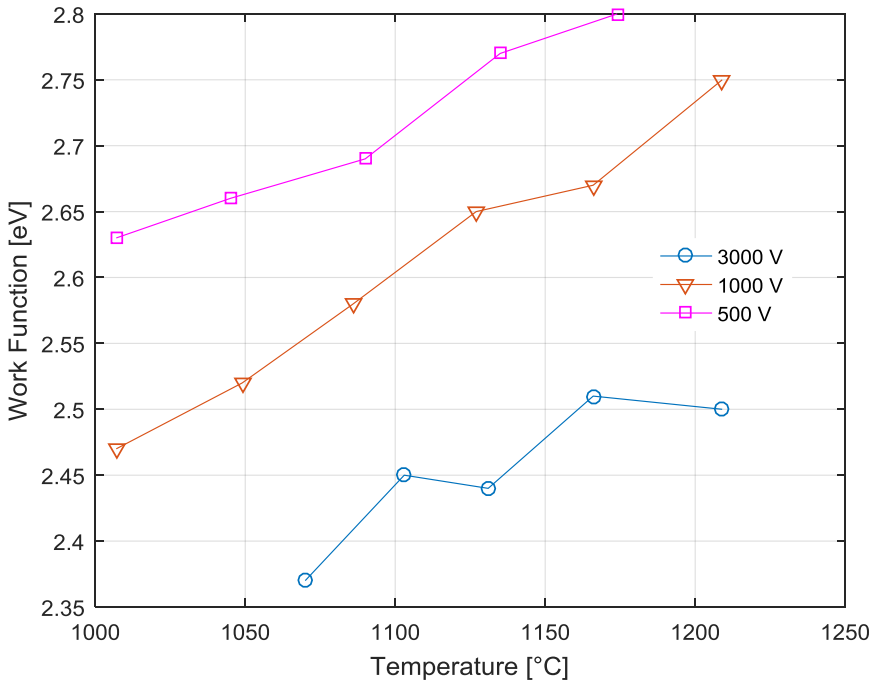

Figure 3.4: Work functions obtained from LWF filaments using the Schottky method.

Recall from Section 1.2.1 that for a thermionic emitter, space-charge effects are observed through a large temperature range within the TL condition. At relatively low voltages, this effect is pronounced and reflected in the deviation from the Richardson-

Dushman curve toward the SCL-TL knee curve, but as voltages increase, the deviation becomes smaller as space-charge effects are mitigated. The difference in measured work functions, seen in Figure 3.4, from 500 V to 3000 V shows this influence of space-charge which can mask an emitter's actual work function by reducing this emission collected for a given temperature. The low voltage measurements can provide an estimate to the emitter's work function [5], but for greater accuracy, electric fields stronger than what is present at 3000 V are necessary to further reduce space-charge effects. It is possible that, based on the data trend of calculated work functions at 3000 V, the lowest work function for this device could agree with published values reported by Capece [6], but this is not expected due to an un-optimized orifice pattern and only a partial seal between the foil enclosure and filament.

A comparison of emission data collected from test articles with an array of diffusion orifices formed by mechanical drilling and laser-burned methods is shown in Figure 3.5. Both filaments used ion-beam polished cermets that were conditioned using sequence #2 and were tested at 500 V. Data points recorded from the laser-burned filament showed a maximum emission current difference of ~32 mA at ~1200°C and a minimum of ~4 mA at 1086°C which are ~37% and ~12%, respectively, less than the drilled filament. The emission current differences between both test articles see a large divergence at 1174°C. It is possible that a portion of this discrepancy can be attributed to the loss of barium vapor escaping through gaps between the tantalum foil basket and filament. The poor seal, due to hastily assembling the test article (see Figure 3.6), allowed barium vapor to bypass the diffusion orifices in the emitter and condense onto cooler surfaces within the electron gun

assembly. This loss mechanism may have been exacerbated above 1174°C because of the detachment of the foil basket.

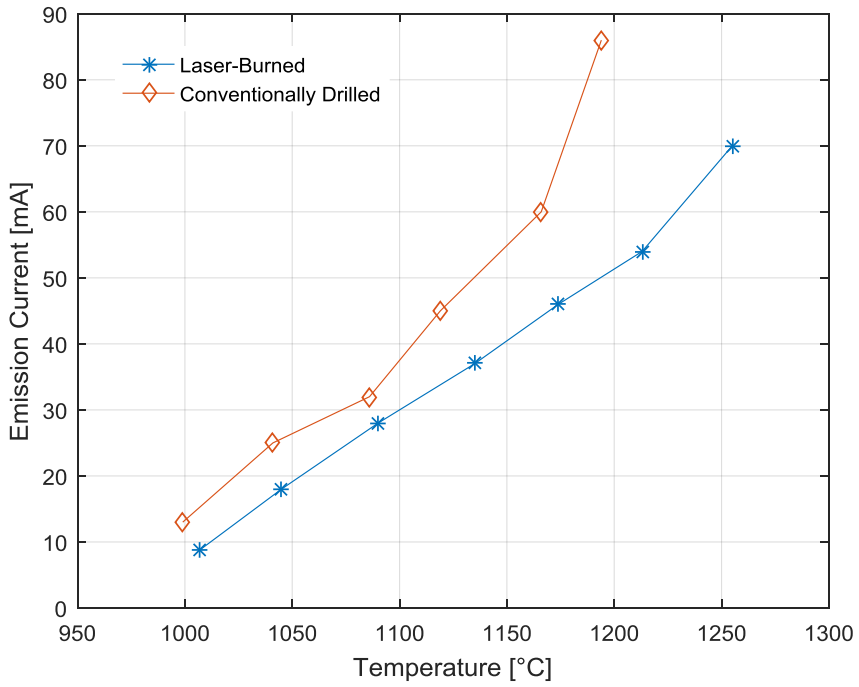

Figure 3.5: Emission variance from filaments formed with laser-burned and mechanically drilled methods. Both were tested at 500 V.

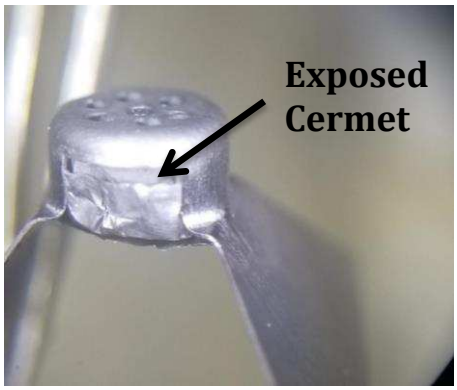

Figure 3.6: Photo showing the gap between the detached tantalum foil basket and filament that allowed the escape of barium vapor.

The barium vapor loss created difficulties in reconciling its impact on the emissive potential of the laser-burned test article, but from a molecular interaction standpoint, neither formation process should present an impediment to forming $Ba^{+}O^{-}$ dipoles on the common tantalum substrate. The ability to collect emission currents without persistent arcing events, however, did favor test articles with laser-burned diffusion orifices. As it will be discussed in the last section of this chapter, laser-burned filaments were found to produce more stable emission currents than conventionally drilled filaments, which, because of the presence of sharp surface blemishes, were more prone to arcing. The abrupt end to data points for the mechanically drilled filament after 1200°C was a result of persistent arcing events, which prevented the collection of useful electron emission data.

Figure 3.7 presents data for cermets tested with front-facing surfaces prepared in as-fired, ion-beam polished, and dry-polished conditions. The relatively poor emission currents collected from the dry-polished cermet likely arose due to the fine grit particles from the abrasive used to treat the insert becoming lodged in surface-level pores of the tungsten matrix, which may have restricted the flow of barium vapor. It is unlikely that cathode poisoning from these particles played a role due to the common materials present in both the cermet and the alumina sandpaper. The data collected for the ion-beam polished cermet is taken from the laser-burned filament presented in Figure 3.5, and again, the depressed emission may be partially accounted for by barium vapor leakage. When compared to the as-fired cermet after a cross-over point at ~1090°C, the divergence in ion-beam polished emission currents can also be explained by differences in the space-charge effects on the filaments. The as-fired cermet, which was tested with a larger voltage and, consequently, a stronger electric field (5.8×10^5 V/m) than the ion-beam polished cermet

(3.4 x 10^5 V/m), experienced a reduced influence from space-charge consequently allowing for greater electron emission. Space-charge effects and barium vapor leakage make it difficult to compare inserts at temperatures greater than 1090°C, but inspection of data points at lower temperatures allows for a slightly clearer analysis since electron emission is affected less by space-charge and more by the temperature-limited condition. Between ~1000°C and 1090°C it is observed that in spite of the vapor leakage, the ion-beam polished cermet produces a slightly larger emission current density than the as-fired insert. The largest difference observed was ~4 mA at ~1050°C – a ~28% increase over the as-fired cermet. This lends some credence to the possibility that non-trivial pore obstructions present in as-fired cermets prevent as much liberation of barium vapor to the emitting surface.

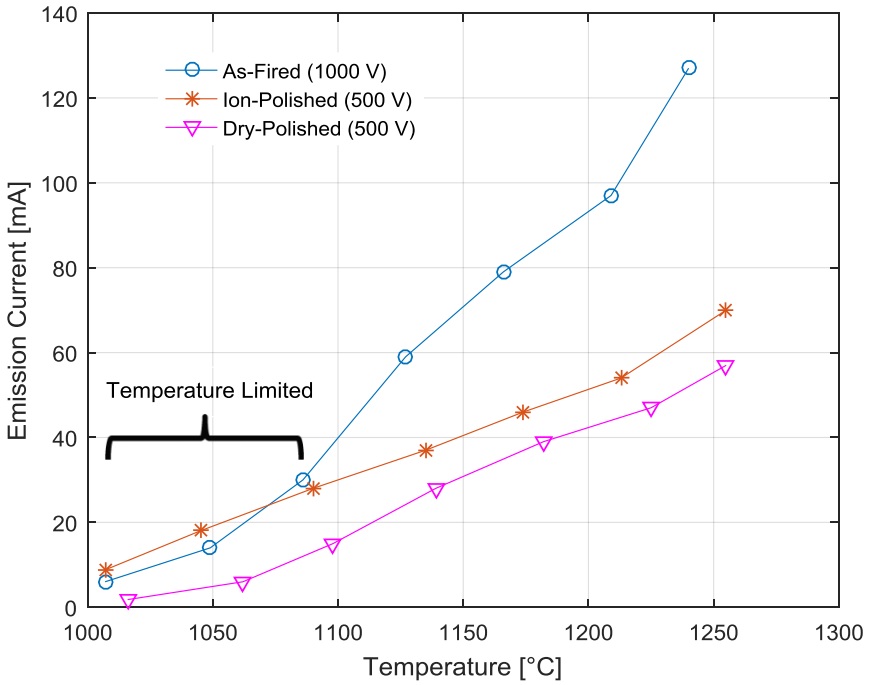

Figure 3.7: Emission variance between as-fired, ion-beam polished, and dry-polished surface finishes on cermets.

Air exposures had a noticeable effect on reducing the emission collected from filaments. Figure 3.8 presents data collected from an initial baseline test along with electron emission following first and second exposures to air. The filament consisted of an as-fired cermet with laser-burned diffusion orifices that was tested at 1000 V. During exposures the chamber was vented with air, but internal components remained untouched. Prior to each test, the cermet was conditioned with sequence #2 after reaching hard vacuum. After performing the initial test, the filament was allowed to cool for 40 minutes. Despite the cooldown period, which should have allowed airborne contaminants to harmlessly adsorb to the cooled cermet, emission currents decreased in the second test. This indicates that the cermet was poisoned by the reintroduction of air or that the seal between the basket and filament became compromised during the test. Emission currents begin to show at sharp increase at 1190°C with currents reaching ~79 mA at 1228°C. The upward trend of the data suggests that the recovery of emission currents is possible following air exposure but may require conditioning or reactivation schedules that may exceed the existing sequences in both temperature and length of time. This is assumed given that the emission currents observed after the first air exposure remained short of that measured in the initial test (127 mA) at a similar temperature and occurred at the end of a ~100 minute test. The filament was allowed to cool for 30 minutes before its second exposure to air. The subsequent test produced emission currents slightly greater than the preceding test. The similarity in data suggests that the impact of air exposures on emission currents may be predictable if the conditions of the exposure are controlled and consistent. The test article, in a similar fashion to the first exposure, began to recover emission

currents, after another ~100 minute test, as the temperature reached 1232°C and registered an emission current of 85 mA.

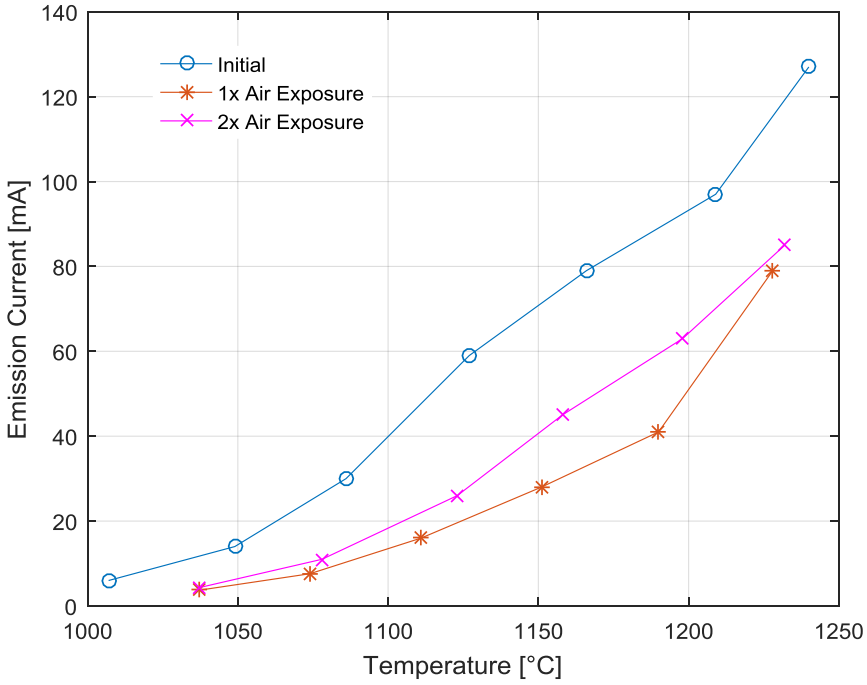

Figure 3.8: Emission variance in an as-fired cermet after two exposures to air.

3.3 Comparison to Analytical Model

As mentioned in Chapter 2, an emission model was developed for use as a tool in refining designs of the LWF filament that solved surface diffusion, work function, and emission equations over a range of temperatures. A general agreement between the calculated and observed emission currents is observed for test articles that did not involve exposures to air, and the discrepancies seen are attributed to the design of the filaments, the testing apparatus, and the model itself.

The filament, which consisted of a dry-polished cermet in a laser-burned filament with seven .010" diameter holes, was tested at 500 V with a filament-to-anode gap of

~.047" – equivalent to a SCL emission density of ~1 A/cm^2. Figure 3.9 presents data collected from the test article overlaid on a plot of both the TL and SCL emission current density models with parameters adjusted to reflect the testing conditions. Emission data stayed within the boundary of the TL curve but noticeably did not reach even 50% of the expected emission density within the temperature range typically cited for barium ceramic impregnated cathodes. In fact, current densities continue to increase slowly past 1300°C. This behavior is likely due to the depressed emission currents caused by pore obstructions in dry-polished cermets or by un-optimized orifice geometry.

The SCL-TL knee terminates at 1300°C due to discretization limits for the time variable in the MATLAB code. A shape factor of 0.5 was applied to Equation 2.6 to fit the SCL-TL knee to the data, which was surprising given that values as low as 1.0 are associated with cathodes that logged close to 60,000 hours of operation and experienced diminished barium coverage uniformity [7]. This, however, makes some sense when considering that restricted barium flow from the dry-polished cermet and vapor loss through the basket enclosure and filament seal would negatively affect the surface uniformity on the emitter. The notable lack of a knee (or a very broad and rounded knee) in the data, which typically indicates a wide variation in work function or uneven loading, also corroborates the shape factor. It is also important to note that Longo's data, presented as a function of time (in kilohours), indicates that early life operation of some cathodes do see low shape factors before eventually increasing after ~5000 hours of operation. These low shape factors may have been associated with emission data collected during an activation schedule employed by Longo. Given that the emission data shown in Figure 3.9 were collected from a filament tested for no longer than 90 minutes, this would imply that these

cermets may require a longer activation period to observe a greater degree of agreement between the model and actual emission data in the SCL-TL knee with shape factors that are more appropriate for a lightly used cermet.

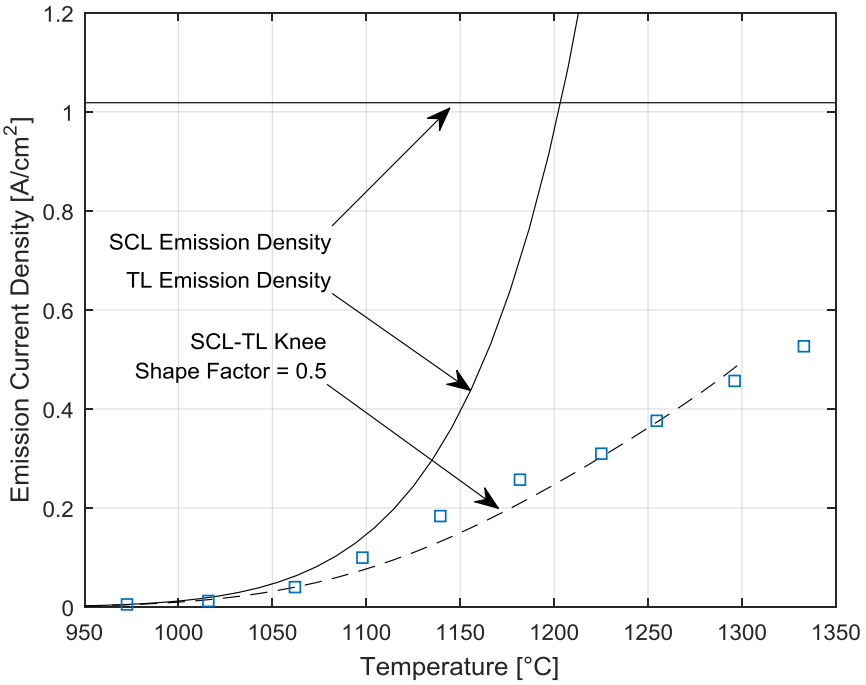

Figure 3.9: Emission current density data points collected at 500 V overlaid on the MATLAB model.

Discrepancies were observed with other test articles when their data was overlaid on TL and SCL models. In some instances, particularly in the TL condition, emission would be greater than the model's prediction. This excess is partially because the model returns a conservative estimation of electron emission due to the method of partitioning the emitting surface (refer to Figure 2.13). And similar to the under estimation of the SCL emission density discussed earlier, an inaccurate measurement of filament-to-anode spacing (skewing slightly larger) would also reduce the contribution of the electric field (and the corresponding emission enhancement due to the Schottky effect) and would be reflected in

the model as a shift down and toward a slightly flatter TL curve. The data presented in Figure 3.9 is also representative of one of a few test articles in which emission data in the SCL condition was collected. Most data and model fits were limited to the TL condition of the filament where in many cases, arcing at higher temperatures prevented the acquisition of reliable data points.

3.4 Additional Observations

Arcing to the anode and Wehnelt cathode from the filaments was an issue that was present throughout testing and was primarily caused by blemishes on the emitter and the subsequent vaporization and ionization of adsorbed contaminants from the anode. The surface blemishes, in the form metal whiskers or sharp corners resulting from holes formed by conventional machining methods, was a primary reason why arcing was a persistent issue with drilled filaments. Arcing occurred to a lesser degree in laser-burned filaments even though dross produced from this process would dome out from the emitting surface. These irregularities caused distortions in electric fields near the surface of the cathode that resulted in the field emission of electrons [8, 9]. When combined with work function reducing barium, these blemishes were able emit in relatively weak electric fields [10] which vaporized and then ionized water or oxygen present on the anode or sublimated portions of the copper anode itself. Vacuum breakdown occurred shortly thereafter if a sufficient amount of contaminants were ionized. Despite the use of water-cooling, high energy electron bombardment of the anode at high currents resulting in elevated temperatures at the area of impact may have melted parts of the anode and contributed to the vacuum breakdown through the same vaporization and ionization mechanisms mentioned above. Ultimately certain measures to eliminate or reduce the

initiation of arcs were put into place including removing the Wehnelt cathode, polishing the surface of the emitters, using an anode with higher melting points and lower sputter yields, and limiting the pulse bias time for applying the voltage ramps to the cathode.

Vacuum breakdown and arcing were not always certain if ionization of anode-borne contaminants occurred. Though not reported earlier in this chapter, the limited ionization of contaminants caused the decay of emission currents over durations of less than 5 seconds. The decay occurred when ionized molecules backstreamed towards the filament, adsorbing to the emitting surface [11, 12, 13]. The adsorbed contaminant locally prevented the diffusion of barium creating patches on the emitter absent of $Ba^{+}O^{-}$ dipoles essentially poisoning the filament. As more of the ionized contaminant migrated to the filament, electron emission steadily decreased. This behavior was observed at temperatures as low as 950°C when sufficiently high voltages were applied to the cathode.

References

[1] Brodie, I. “Emission Fluctuations of Tungsten-Based Barium Dispenser Cathodes.” *Journal of Applied Physics* 32, no. 10 (1961): 2039-2046.

[2] Rittner, E.S. “On the mechanism of operation of the type B impregnated cathode.” *Journal of Applied Physics* 48, no. 10 (1977): 4344-4346.

[3] Langmuir, Irving. “The Interaction of Electron and Positive Ion Space Charge in Cathode Sheaths.” *Physical Review* 33, no. 6 (1929): 954-989.

[4] Forman, R. “Surface studies of barium and barium oxide on tungsten and its application to understanding the mechanism of operation of an impregnated tungsten cathode.” *Journal of Applied Physics* 47, no. 12 (1976): 5272-5279.

[5] Rubin, Binyamin, and John D. Williams. "Hollow cathode conditioning and discharge initiation." *Journal of Applied Physics* 104, no. 5 (2008): 053302.

[6] Capece, Angela M., James E. Polk, and Joseph E. Shepherd. "Decoupling the Thermal and Plasma Effects on the Operation of a Xenon Hollow Cathode With Oxygen Poisoning Gas." *IEEE Transactions on Plasma Science* 43, no. 9 (2015): 3249-3255.

[7] Longo, R.T. “Physics of Thermionic Dispenser Cathode Aging.” *Journal of Applied Physics* 94, no. 10 (2003): 6966-6975.

[8] Melmed, A.J, and R. Gomer. “Field Emission from Whiskers.” *The Journal of Chemical Physics* 34, no. 5 (1961): 1802-1812.

[9] Boyle, W.S., P. Kisliuk, and L.H. Germer. “Electrical Breakdown in High Vacuum.” *Journal of Applied Physics* 26, no. 6 (1954): 720-725.

[10] Brodie, I. “Vacuum Breakdown in the Presence of Thermionic Cathodes.” *Journal of Vacuum Science and Technology* 2, no. 5 (1965): 249-256.

[11] Marrian, C.R.K., G.A. Haas, and A. Shih. “Fast turn-on characteristics of tungsten-based dispenser cathodes following gas exposures.” *Applications of Surface Science* 16, no. 1-2 (1983): 73-92.

[12] Deb, S. “Decay of emission from an oxide-coated cathode due to adsorption of matter liberated from the anode.” *Journal of the British Institution of Radio Engineers* 14, no. 4 (1954): 157-167.

[13] Feaster, G.R. “Pulse Emission Decay Phenomenon in Oxide-Coated Cathodes.” *Journal of Applied Physics* 20, no. 4 (1949): 415-416.

4 Conclusion and Future Work

4.1 Conclusion

Evaporation and thermally-induced distortions of tantalum filaments are the prominent runtime-limiting factors of EBAM units. The research presented in this thesis explored a means to extend the operational duration of these filaments beyond their typical 4 hour life by marrying it with a low work function material to reduce its operating temperature without compromising the minimum electron emission current required for production. In this regard the combination of these two technologies was shown to meet the beam current requirements of EBAM systems and exceed the existing runtime limitations. However, further investigation into the fabrication of the LWF filament, specifically optimizing the array of barium diffusion orifices and hermetically sealing the foil enclosure to the filament, is required and addressed here and in the following sub-section.

EBAM systems require 200 mA beam currents to engage in printing campaigns, and it was found that LWF filaments could maintain this condition with heater currents no greater than 40 A, equivalent to ~1200-1225°C, for 75 hours – more than 18 times longer than a standard, unmodified filament. Plasma exposure aided in the increased emission currents but results from a subsequent, voluntarily terminated 8.5 hour test in a purely vacuum test setting corroborated these findings. The vacuum test also produced an emission current density of ~1.07 A/cm^2 which, when accounting for Schottky enhancement effects, can be expected to increase to ~1.41 A/cm^2 - exceeding the nominal operating emission current density of 1.29 A/cm^2 for EBAM units. The full activation of

cermets, seen in both the plasma and vacuum emission tests, will also aid to enhance electron emission.

Emission characteristics between conventionally drilled and laser-burned filaments were studied and the data collected were found to be inconclusive due largely to barium vapor leakage from a gap between the foil enclosure basket and filament. The leakage accounted for differences in emission current density as high as ~37%. Despite this, the molecular interactions between barium, oxygen, and the tantalum substrate that form work function reducing dipoles should not be affected by diffusion orifice formation methods. Conventionally drilled filaments, however, have shown a comparatively higher sensitivity to arcing events because its formation process produces surface blemishes and metal whiskers that distort and locally increase electric fields which initiate arcs at voltages as low as 300 V. This effect is exacerbated with adsorbed barium and oxygen. These blemishes may be removed through careful polishing or electrical conditioning procedures, but stable emission currents at greater potentials through the comparatively more convenient method of laser-burning may be the more attractive option despite the presence of dross.

The surface finish on inserts have considerable influence on the emissive capability of LWF filaments particularly in the case of dry-polished cermets, which display notably depressed electron emission currents compared to other surface conditions presumably due to obstructed pores. At temperatures less than 1090°C, ion-beam polished cermets produced emission currents slightly greater than as-fired inserts with a maximum observed increase of 4 mA. A 500 V difference in testing potential produced dissimilar space-charge effects in the two filaments, but this behavior presumably applies to

temperatures greater than 1090°C as well. While greater emission currents were collected from the ion-beam polished cermet, the additional 20+ hours required in its preparation does not justify this marginal increase. Instead, a filament using an as-fired cermet can be expected to produce emission currents, in conjunction with Schottky enhancement and full activation of the cermet, more than sufficient for EBAM applications.

An investigation on the effect of air exposures on cermet emission currents found that, following a 40 minute cooldown period, barium ceramic tungsten cermets can still experience decreased emission currents due to poisoning or vapor sealing degradation. Extended cooldown periods may diminish this effect but may also result in undesirably longer printing delays. It was found, however, that despite the poisoning, emission currents may be recoverable after observing currents from the first and second exposures to air sharply increase to within ~33% of the initial test's emission current at 1240˚C after ~100 minutes of testing. To fully recover the performance of the cermet, a modification of the conditioning and reactivation sequence may be required to elevate the temperature of the filament past that which is typical at a 40 A heating current.

A model used to predict emission currents from these LWF filaments was developed and found to have an acceptable level of agreement with test articles in steady-state, temperature limited conditions. Large emission deviations from the TL curve were explained by a restricted supply of barium vapor from the dry-polished cermet or barium vapor lost through a poor seal between the foil enclosure basket and filament. A shape factor of 0.5, which indicates poor surface uniformity, was used to fit the SCL-TL knee to data points. This agrees with the physical condition of the LWF filament, which was either

insufficiently activated or experienced a throttled barium supply from restriction or loss mechanisms that, in turn, affected the uniformity over the emitter's surface.

4.2 Directions for Future Work

The quality of construction of LWF filaments, though improved over the course of this research, could be more carefully assembled for additional testing. Specifically, laser welding the enclosure basket for the barium ceramic cermet to the filament would help to eliminate barium vapor loss. In addition the array of diffusion orifices could be formed with a more sophisticated laser-burning procedure that does not produce dross, or alternatively, new methods of forming the array of holes such as selective ion beam or photoresist etching could be explored.

Further studies on the conditioning and activation of ion-beam polished cermets for both initial test runs as well as after exposures to air need to be explored. Further, should arcing still present an issue with the operation of filaments, tests conducted with increased electrode gaps and higher voltage supplies could be employed. Concurrently, further refinement of the emission model with a thoroughly activated filament could be investigated along with comparisons to transient behavior, which the model is currently capable of doing.

The operation of LWF filaments in production will likely require a change in control methodologies. Presently EBAM systems operate in the space-charge limited condition and control the negative bias applied to the Wehnelt cathode to set the electron emission current as needed. The LWF filament operates in the temperature-limited condition and, in addition to the Wehnelt cathode, requires control of the heater current to manage barium

surface coverage. An investigation into the adaptation of current EBAM control methodologies to operate these new filaments suitably would be invaluable.

5 Appendix A: BaO-CaO-Al_2O_3 Decomposition

The barium oxide ceramic is only half of a dispenser cathode, which also requires a porous, tungsten metal matrix that not only provides structure and pathways through which barium vapor can diffuse but also aids in the reduction of barium calcium aluminate into barium vapor. Rittner studied the loss of barium from a 5:3:2 dispenser cathode and observed that barium loss from the impregnated insert was in agreement with the following chemical reaction [1]:

$$5BaO * 3CaO * 2Al_2O_3(s) + \frac{3}{4}W(s) \rightarrow \frac{3}{4}Ca_2BaWO_6(s) + \frac{3}{4}Ca_2BaAl_2O_6(s) + \frac{5}{4}BaAl_2O_4(s) + \frac{9}{4}Ba(g) \quad (5.1)$$

Lipeles later expounded on this reaction explaining that the thermal decomposition of BaO into vapor form and its subsequent reaction with the tungsten matrix produced barium tungstate, $Ba(WO_6)$, and a portion of the atomic barium vapor seen in Rittner's reaction (Equation 5.2). The remainder of the barium vapor produced in Rittner's model comes from the further reduction of the barium tungstate (Equation 5.3) [2]. It should be noted that not all of the gaseous barium oxide necessarily needs to be reduced to atomic barium vapor as BaO (g) is also capable of creating the required dipole on the tungsten substrate.

$$2BaO(g) + \frac{1}{3}W(s) \rightarrow \frac{1}{3}Ba_3WO_6(s) + Ba(g) \quad (5.2)$$

$$\frac{1}{2}Ba_3WO_6(s) \rightarrow \frac{1}{2}BaWO_4(s) + BaO(g) \quad (5.3)$$

Lipeles also reported that in addition to barium vapor, calcium oxide would reduce in similar reactions as barium oxide to release calcium and oxygen vapor and would be liberated through the reactions:

$$CaO(g) \rightarrow Ca(g) + \frac{1}{2}O_2(g) \tag{5.4}$$

$$2CaO(s) + \frac{1}{3}W(s) \rightarrow \frac{1}{3}Ca_3WO_6(s) + Ca(g) \tag{5.5}$$

References

[1] Rittner, E.S. “On the mechanism of operation of the type B impregnated cathode.” *Journal of Applied Physics* 48, no. 10 (1977): 4344-4346.

[2] Lipeles, R.A., and H.K.A. Kan. “Chemical stability of barium calcium aluminate dispenser cathode impregnants.” *Application of Surface Science* 16, no. 1-2 (1983): 189-206.

6 Appendix B: Dipole Interactions

The dipole interactions between the cathode's metal substrate and the liberated oxygen and barium, as shown in Figure 6.1, are products of their electronegativities, and by extension their valence electrons, and the strength of their resulting desorption energies [1]. Cathodes made from tungsten or tantalum are moderately electronegative (2.36 and 1.5 on the Pauling scale, respectively) and are likely to form a dipole with a strongly electronegative (3.44) oxygen atom. The electron shared between the two molecules is pulled closer to the oxygen atom effectively making it more negative and the substrate more positive. The monolayer of oxygen that ultimately forms on the substrate possesses high desorption energies, which for tungsten can range between 6.1 to 6.5 eV [1]. Adsorbed oxygen atoms remain strongly electronegative, requiring two electrons to completely fill its outer electron shell, and thus attract less electronegative barium atoms that are likely to give up a valence electron. The monolayer of barium lying on the existing oxygen monolayer is bonded with another strong dipole that leaves the barium more positively charged. This creates a favorable condition described by Jenkins [2] as an electropositive layer that reduces the work function of the cathode's surface to ~2.1 eV. The subsequent thermionic emission is the result of the remaining valence electron escaping the outer shell of the barium atom. Eventually the portions of the barium monolayer that have expelled their remaining valence electron evaporate from the cathode's emitting surface and condense onto cooler surfaces [3]. The vacancies that are created are filled by diffusing barium molecules released from the impregnated insert.

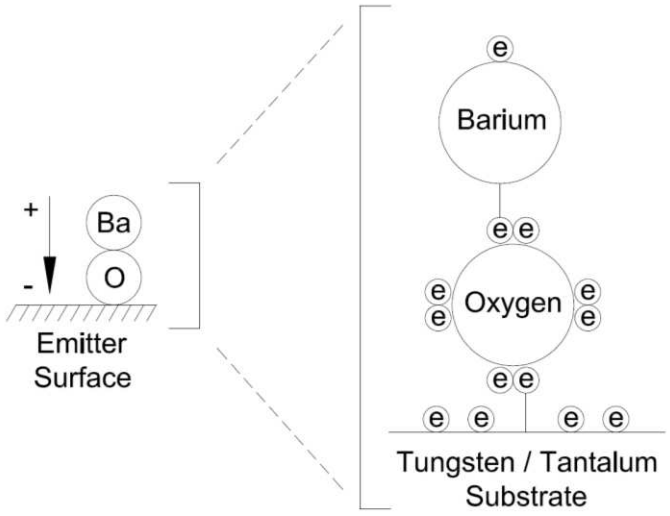

Figure 6.1: A schematic illustrating valence electron interactions in $Ba^{+}O^{-}$ dipoles.

Other dipole configurations are possible with barium and oxygen that create localized patches of typically higher work functions. The metal substrate-oxygen dipole absent of any barium is a likely dipole that would arise in situations where the impregnated insert has either not been thermally activated to a temperature that would produce barium vapor, has been poisoned through improper conditioning, has blockages in the porous tungsten matrix, or is close to exhausting its supply of barium. A dipole consisting of a second monolayer of oxygen in place of barium can, for tungsten cathodes, produce volatile tungsten oxides that have the potential to cause cathode failures [1]. Oxygen, or any other vapors that are present (due either to poor vacuum conditions, sputtered or sublimated metals), can also create a third monolayer on top of the barium effectively increasing the work function of the cathode [1]. Polk refers to this dipole interaction as a cathode poisoning mechanism as well. Multiple monolayers of barium are also possible but likely to rapidly evaporate in bulk [4]. A final possible dipole, though less likely due to the constant presence of oxygen, is one in which a barium monolayer forms over the metal substrate.

Brodie compared barium evaporation rates from cathodes in the presence of oxygen [5] to data collected by Moore and Allison for evaporation rates from clean tungsten surfaces absent of oxygen [6]. Brodie observed that cathodes with oxygen monolayer present resulted in lower evaporations rates and were able to maintain full coverage of an overlying barium monolayer whereas the comparatively weaker bond between barium and tungsten resulted in the more rapid desorption of barium. The necessity of oxygen is underscored in the previous examination of the molecular arrangement of the dipole and their respective electronegativities.

References

[1] Polk, James E. "The Effect of Reactive Gases on Hollow Cathode Operation." *42nd AIAA/ASME/SAE/ASEE Joint Propulsion Conference & Exhibit*, (2006): AIAA-2006-5153.

[2] Jenkins, R.O. "A review of thermionic cathodes." *Vacuum* 19, no. 8 (1969): 353-359.

[3] Longo, R.T. "Long life, high current density cathodes." *Electron Devices Meeting, 1978 International*, (1978): 152-155.

[4] Jensen, K.L., Y.Y. Lau, and B. Levush. "Migration and escape of barium atoms in a thermionic cathode." *IEEE Transactions on Plasma Science* 28, no. 3 (2000): 772-781.

[5] Brodie, I., and R.O. Jenkins. "The nature of the emitting surface of a barium dispenser cathodes." *British Journal of Applied Physics* 8, no. 1 (1956): 27-29.

[6] Moore, G.E., and H.W. Allison. "Adsorption of Strontium and of Barium on Tungsten." *The Journal of Chemical Physics* 23, no. 9 (1955): 1609-1621.

7 Appendix C: MATLAB Codes

7.1 Calibration Code

```
%ImportAnalyze_LoggedData_ColdFilaments.m searches for a designated .lvm
%file (file extension for logged data from the National Instruments data
%acquisition device, USB-6002), parses the data, and plots the raw data for
%the high voltage (HV) sweep against the raw data for the system current. The
%resulting linear fit is the characteristic resistance of the system with a
%particular filament installed. The 'slope' and 'intercept' are then taken
%and used to calibrate the data analyzed in
%ImportAnalyze_LoggedData_HotFilament.m

      %%%%%%%%%%%%%%%%%%%   IMPORT & CLEAN DATA   %%%%%%%%%%%%%%%%%

file = 'U:\Grad - Research\Logging Data\Raw Data\#SCLM_16_B_001.lvm';
[pathstr,name,ext] = fileparts(file);   %Break file path into parts
path(pathstr,path)                      %Set path using pathstr
filename = strcat(name,ext)             %Recompose file and extension
range = [23 1 : 3];                     %Specify range of data to import
Raw_Data = dlmread(filename,',',range); %Import data using comma delimiter
FilaNameandTest = strrep(name,'_',' '); %Replaces "_" with a space in
filament name for use in plots

%Search for rows with value = 0 in raw data and delete. These rows come
%from the comment column added into the logged data by the NI DAQ system
junk_row = find(Raw_Data(:,1)==0);      %Search for rows of value 0
Clean_Data = Raw_Data;                  %Separate raw data from cleaned data
Clean_Data(junk_row,:) = [];            %Delete rows

          %%%%%%%%%%%%%%%%%%%   ANALYZE DATA   %%%%%%%%%%%%%%%%%

HV_Sweep = Clean_Data(:,1);             %Voltage sweep in system, [V]
Current = Clean_Data(:,3);              %Total system current, [mA]

trend_coeff = polyfit(HV_Sweep,Current,1);   %linear fit of data, y = mx+b
trendline = polyval(trend_coeff,HV_Sweep);
slope = mat2str(trend_coeff(1))              %convert m into a string
intercept = mat2str(trend_coeff(2))          %convert b into a string
trendline_eqn = strcat({'y = '},slope,{'x + '},intercept);

              %%%%%%%%%%%%%%%%%%%   PLOTS   %%%%%%%%%%%%%%%%%
figure
scatter(HV_Sweep,Current,10,'b'); hold on;
plot(HV_Sweep,trendline)
annotation('textbox',[.35 0 .3
.3],'String',trendline_eqn,'FitBoxToText','on')
title(strcat({'Cold Filament/Baseline System Resistance -
'},FilaNameandTest,{' Filament'}))
xlabel('Applied Voltage (V)')
ylabel('Current (mA)')
legend('0 A (0 deg C) Heater Current','1/R_{eq}')
```

7.2 Data Processing Code

```
%Similar to ImportAnalyze_LoggedData_ColdFilaments.m, _HotFilaments.m
%searches for a designated .lvm file and parses and cleans the raw data for
%high voltage (HV) sweep - either 3000 V or 1000 V depending on the test -
%and system current. The 'slope' and 'intercept' from _ColdFilaments.m for
%a particular filament is entered into the variables named 'slope' and
%'y-inter'. Using the cold filament resistance, the "True" emissions and
%voltage at the filament can be calculated. These are then cleaned of noise
%using a simple digital filter. The "Filtered" emissions and voltage are
%then processed and used to generate Schottky plots (3000 V Sweep)or to
%determine steady state emissions for a Miram curve (1000 V Steady) - made
%in MS Excel. Work functions are calculated using the zero-field saturated
%emission taken from Schottky plots. Processed data can be output as an MS
%Excel file as an option.

   %%%%%%%%%%%%%%%%%%%   ENTER TESTING PARAMETERS   %%%%%%%%%%%%%%%%%

htr_current = 40.0;                     %Heater current, [A]
temp_C = 1311;                          %Filament temp, [deg C]
acc_volt = '3000 V Ramp Acc. Potential';
Test_Parameters = strcat(num2str(htr_current),{' A
('},num2str(temp_C),{' deg C)'});

   %%%%%%%%%%%%%%%%%%%   ENTER FILAMENT PARAMETERS   %%%%%%%%%%%%%%%%%

n_holes = 5;                        %Number of holes in filament
r0 = 0.010;                         %Radius of holes, [in]
d_in = 0.125;                       %Filament-anode distance, [in]
      %%%%%%%%%%%%%%%%%%%   IMPORT & CLEAN DATA   %%%%%%%%%%%%%%%%%

%Locate and import logged data
file = 'U:\Grad - Research\Logging Data\Raw Data\#SCLM_16_B_002.lvm';
[pathstr,name,ext] = fileparts(file);   %Break file path into parts
path(pathstr,path)                      %Set path using pathstr
filename = strcat(name,ext)             %Recompose file and extension
range = [23 1 : 3];                     %Specify range of data to import
Raw_Data = dlmread(filename,',',range); %Import data using comma delimiter
and range
FilaNameandTest = strrep(name,'_',' '); %Replaces "_" with a space in
filament name for use in plots

%Search for rows with value = 0 in raw data and delete. These rows come
%from the comment column added into the logged data by the NI DAQ system
junk_row = find(Raw_Data(:,1)==0); %Search for rows of value 0
Clean_Data = Raw_Data;              %Separate raw data from cleaned data
Clean_Data(junk_row,:) = [];        %Delete rows

          %%%%%%%%%%%%%%%%%%%   ANALYZE DATA   %%%%%%%%%%%%%%%%%

HV_Sweep = Clean_Data(:,1);         %Voltage sweep in system, [V]
Current = Clean_Data(:,3);          %Total system current, [mA]

%Cold Filament Resistance - characterization of system resistance with a
%filament installed that has no heating current applied
slope = 0.483562807498981;          %Value must be updated for each filament
```

```
y_inter = 7.9947791088866;        %Value must be updated for each filament
R_inline = 501;                   %Inline resistor, [ohms]

%Emissions and voltage associated with the filament
True_Emissions = Current - (slope.*HV_Sweep - y_inter);
True_Voltage = HV_Sweep - True_Emissions*(R_inline/1000);

%Simple digital filtering for data
R = 0.05;                         %R=1, no filtering; R=0.01, lots of filtering
R_filter = num2str(R);            %Converts filtering factor to a string
Data_filter = strcat({'Data Filtering, R = '},R_filter);

for n = 2:length(True_Emissions)
Filtered_Emissions(1) = True_Emissions(1);
Filtered_Emissions(n) = True_Emissions(n)*R+(1-R)*Filtered_Emissions(n-1);
Filtered_Voltage(1) = True_Voltage(1);
Filtered_Voltage(n) = True_Voltage(n)*R+(1-R)*Filtered_Voltage(n-1);
end

Filtered_Emissions = Filtered_Emissions';
Filtered_Voltage = Filtered_Voltage';

Sqrt_Voltage = sqrt(Filtered_Voltage);

%Select specific range to determine avg emissions for use in Miram curve
strt0 = 1000;
stop0 = 2100;
Avg_Emission = mean(Filtered_Emissions(strt0:stop0,1));
Avg_Current = strcat({'Average Emission Current = '},num2str(Avg_Emission),{'
mA'});

%Select specific range for use in Schottky plot
strt1 = 2900;                                 %Specify first value of range
stop1 = 3400;                                 %Specify last value of range
Sqrt_V = [0;Sqrt_Voltage(strt1:stop1,1)];     %Must include 0 to extend range
& get z-field emission
Smooth_E = [0;Filtered_Emissions(strt1:stop1,1)]; %Must include 0 to extend
range & get z-field emission

%Select specific range to identify the Schottky Region.
strt2 = 3100;                                 %Specify first value of range
stop2 = 3400;                                 %Specify last value of range
Schott_Voltage = Sqrt_Voltage(strt2:stop2,1);
Schott_Emission = Filtered_Emissions(strt2:stop2,1);

%Use polyfit with a logarithmic modification to linearly fit the Schottky
%Region and get 1st order trendline coefficients. Take the exponent of
%polyval for the coefficients and the entire range of square-rooted
%voltages to get a linear trendline spanning the entire plot. Determine the
%zero-field current by taking the value from 'trendline' associated with
%zero volts.
trendline_Coeff = polyfit(Schott_Voltage,log(Schott_Emission),1);
trendline = exp(polyval(trendline_Coeff,Sqrt_V));
zfield_emission = trendline(1);                                    %[mA]
zfield_current = strcat({'Zero-Field Emission Current =
'},mat2str(zfield_emission),{' mA'});
```

```
    %%%%%%%%%%%%%%%%%%%%   CALCULATE WORK FUNCTION   %%%%%%%%%%%%%%%%%

A_fila = 1.55e-5;                           %Emitting area of filament, [m^2]
d = d_in*0.0254;                            %filament-anode distance, [m]
A_holes = n_holes*pi*(r0*0.0254)^2;         %total area of holes, [m^2]

temp_K = temp_C + 273;                      %Filament temp, [Kelvin]

q = 1.6e-19;                        %electron charge [C]
k_Boltz = 1.38e-23;                 %Boltzmann's constant, [J/K]
A_Rich = 1.20173e6;                 %Richardson-Dushmann constant, [A/(m^2*K^2)]
Gr = 0.31;                          %Reflection coefficient, Gamma [-]

zfield_Amps = zfield_emission/(A_fila-A_holes)/1000;             %[A/m^2]
phi = -1*temp_K*k_Boltz/q*log(zfield_Amps/A_Rich/Gr/(temp_K^2)); %[eV]
workfxn = num2str(phi);
work_function = strcat({'Work Function = '},workfxn,{' eV'})

              %%%%%%%%%%%%%%%%%%%%   PLOTS   %%%%%%%%%%%%%%%%%

figure;
scatter(Sqrt_V,Smooth_E,10,'b'); hold on;
scatter(Schott_Voltage,Schott_Emission,10,'r');hold on;
plot(Sqrt_V,trendline,'k')
grid
set(gca,'yscale','log')
annotation('textbox',[.3 .15 .3
.3],'String',zfield_current,'FitBoxToText','on')
annotation('textbox',[.3 .075 .3
.3],'String',work_function,'FitBoxToText','on')
annotation('textbox',[.3 0 .3
.3],'String',Test_Parameters,'FitBoxToText','on')
xlabel('Sqrt Voltage (Sqrt V)')
ylabel('Emission Current (Log mA)')
legend('Filtered (R = 0.05) Filament Emissions vs. Collection
Voltage','Schottky Region','Schottky Region Linear Extrapolation')
title(strcat({'Schottky Plot - '},FilaNameandTest,{' Filament'}))

figure;
grid;
yyaxis left
scatter(1:length(Filtered_Voltage),Filtered_Voltage,1)
xlabel('Time Step [ms]');
ylabel('Voltage [V]')
yyaxis right
scatter(1:length(Filtered_Emissions),Filtered_Emissions,1)
ylabel('Emission Current [mA]')
annotation('textbox',[.3 .15 .3
.3],'String',Avg_Current2,'FitBoxToText','on')
annotation('textbox',[.3 .075 .3
.3],'String',Avg_Current1,'FitBoxToText','on')
annotation('textbox',[.3 0 .3
.3],'String',Test_Parameters,'FitBoxToText','on')
title(strcat({'Filtered Voltage & Emission - '},FilaNameandTest,{'
Filament'}))
```

```
figure;
grid;
yyaxis left
scatter(1:length(True_Voltage),True_Voltage,1)
xlabel('Time Step [ms]');
ylabel('True Voltage [V]')
yyaxis right
scatter(1:length(True_Emissions),True_Emissions,1)
ylabel('True Emissions [mA]')
annotation('textbox',[.3 0 .3
.3],'String',Test_Parameters,'FitBoxToText','on')
title(strcat({'True Voltage & Emissions - '},FilaNameandTest,{' Filament'}))

figure;
grid;
yyaxis left
scatter(1:length(HV_Sweep),HV_Sweep,1)
xlabel('Time Step [ms]');
ylabel('Applied Voltage [V]')
yyaxis right
scatter(1:length(Current),Current,1)
ylabel('System Current [mA]')
annotation('textbox',[.3 0 .3
.3],'String',Test_Parameters,'FitBoxToText','on')
title(strcat({'System Voltage & Currents - '},FilaNameandTest,{' Filament'}))

figure
plot(strt0:stop0,Filtered_Emissions(strt0:stop0))
annotation('textbox',[.3 .15 .3 .3],'String',Avg_Current,'FitBoxToText','on')
annotation('textbox',[.3 .075 .3
.3],'String',Data_filter,'FitBoxToText','on')
annotation('textbox',[.3 0 .3
.3],'String',Test_Parameters,'FitBoxToText','on')
xlabel('Time Step (ms)')
ylabel('Filtered Emissions (mA)')
title(strcat({'Miram Data - Avg Emissions - '},FilaNameandTest,{'
Filament'}))
```

7.3 Emission Model Parent Code

```
function LWF_Filament_VarTemp

% Bao Nguyen, 14 Dec 2017, Colorado State University

% Function Summary:
% LWF_Filament_VarTemp is a "parent" code that passes values for temperature,
% T [K], hole qty, n, hole size, dia [in], voltage, V, and anode distance,
% d [m], as arguments to the "child" code, LWF_Filament_VarParam. The
% arguments passed are single valued except for the temperature which can be
% a range of values. LWF_Filament_VarParam returns values for temperature
% limited emissions, Ie_TL [A], and effective work function, wfunc [eV].

%%%%%%%%%  SIMULATION PARAMETERS  %%%%%%%%%

% Filament configuration
dia = 0.010;                % hole diameter [in]
n = 7;                      % number of holes
dia_f = 0.175;                                  %Diameter of filament
emitting surface, [in]
a_f = ((pi/4)*((dia_f^2)-n*(dia^2)))*(2.54^2);  %Area of filament emitting
surface, [cm^2]

HoleSize = strcat(num2str(dia),' in Hole Dia.');
HoleQty = strcat(num2str(n),' Holes');

% Electric field
V = 500;                    % filament-anode voltage [V]
d_in = 0.063;               % filament-anode distance [in]
d = d_in*0.0254;            % filament-anode distance [m]
Voltage = strcat(num2str(V),' V Acc. Potential');
Distance = strcat(num2str(d_in),' in Anode Distance');

% Temperature range
T_c_lo = 950;               % lower bound, filament temp [deg C]
T_c_hi = 1300;              % upper bound, filament temp [deg C]
T_lo = T_c_lo + 273;        % lower bound, filament temp [K]
T_hi = T_c_hi + 273;        % upper bound, filament temp [K]
Tsteps = 10;                % temperature increments
T = linspace(T_lo,T_hi,(T_hi-T_lo)/Tsteps); % temp range in for-loop
T_c = T - 273;

%%%%%%%%%  LOAD EXPERIMENTAL DATA  %%%%%%%%%

load SCLM_30                          %Import emission data
Meas_Temp = SCLM_30(2:20,1);          %Test temp for emission [deg C]
Meas_Ie_mA = SCLM_30(2:20,2);         %Measured emission [mA]
Meas_Je = Meas_Ie_mA/1000/a_f;        %Measured emission density [A/cm^2]

% load SCLM_18                        %Import emission data
% Meas_Temp = SCLM_18(:,1);           %Test temp for emission [deg C]
% Meas_Ie_mA = SCLM_18(:,2);          %Measured emission [mA]
% Meas_Je = Meas_Ie_mA/1000/a_f;      %Measured emission density [A/cm^2]

% load SCLM_27_1x                     %Import emission data
```

```
% Meas_Temp1 = SCLM_27_1x(:,1);        %Test temp for emission [deg C]
% Meas_Ie1_mA = SCLM_27_1x(:,2);       %Measured emission [mA]
% Meas_Je1 = Meas_Ie1_mA/1000/a_f;     %Measured emission density [A/cm^2]

% load SCLM_27_2x                      %Import emission data
% Meas_Temp2 = SCLM_27_2x(:,1);        %Test temp for emission [deg C]
% Meas_Ie2_mA = SCLM_27_2x(:,2);       %Measured emission [mA]
% Meas_Je2 = Meas_Ie2_mA/1000/a_f;     %Measured emission density [A/cm^2]

%%%%%%%%%  CALCULATIONS  %%%%%%%%%

% Solves for TL emissions, Ie_TL [A], and eff. work function, wfunc [eV}
for i = 1:length(T)
    [Ie_TL(i),wfunc(i)] = LWF_Filament_VarParam(T(i),dia,n,V,d);
end

% Percentage of space charge limited current. Used in Miram curves.
for i = 1:length(Ie_TL)
    SCL_Pct(i) = Ie_TL(i)/Ie_TL(end);
end

% Emission density
Je_TL = Ie_TL/a_f;
Je_density = Ie_TL(end)/a_f;          %Calc'd emission density [A/cm^2]
Current_density = strcat(num2str(Je_density),' A/cm^{2})');

%%%%%%%%%  CALCULATE SCL CURRENT BASED ON PARAMETERS  %%%%%%%%%

% Solves the 1-D Child-Langmuir Law for the SCL current density,
% Je_SCL [A/m^2], and the max emission current, Ie_SCL [A], for the filament
% with diameter, dia_f [in], hole diameter, dia [in], and number of holes,
% n, for the specified voltage and filament-anode gap
A_fila = pi*((dia_f/2)*0.0254)^2;     %Emitting area of filament, [m^2]
A_holes = n*pi*((dia/2)*0.0254)^2;    %total area of holes, [m^2]
q = 1.6e-19;                          %electron charge [C]
m_q = 9.109e-31;                      %electron charge mass [kg]
e0 = 8.854e-12;                       %vacuum permittivity [F/m]

SCL_constant = e0*(4/9)*(sqrt(2*(q/m_q)));

Ie_SCL = SCL_constant*((V^(3/2))/(d^2))*(A_fila-A_holes)     %[A]
Je_SCL_m2 = SCL_constant*((V^(3/2))/(d^2))                   %[A/m^2]
Je_SCL = Je_SCL_m2/(100^2)                                   %[A/cm^2]
SCL_Emission = strcat(num2str(Je_SCL),' A/cm^2')

%%%%%%%%%  SCL-TL KNEE  %%%%%%%%%

% Use Eqn 7 from Longo, R.T., "Physics of thermionic dispenser cathode
% aging", (2003) to estimate emissions in the SCL-TL knee. Shape factor is
% selected to fit the transition to the collected data
a = 0.5;                              %Shape factor, alpha [-]

for i = 1:length(Je_TL)
    Je_TOT(i) = ((1/(Je_SCL^a))+(1/(Je_TL(i)^a)))^(-1/a);
end

%%%%%%%%%  PLOTS  %%%%%%%%%
```

```
deg = char(0176);

figure;
plot(T_c,Je_TL,'-k'); hold on
plot(T_c,Je_TOT,'--k'); hold on
% plot(T_c,Ie_TOT1,'--k'); hold on
line([900 1600],[Je_SCL Je_SCL],'Color','black','Linestyle','-'); hold on
% line([T_c_lo T_c_hi],[Ie_SCL1 Ie_SCL1],'Color','black','Linestyle','-');
hold on
% text(T_c_lo+25,Je_SCL+.025,SCL_Emission)
% text(1010,Ie_SCL1+.025,SCL1_Emission)
plot(Meas_Temp,Meas_Je,'s'); hold on
% plot(Meas_Temp1,Meas_Je1,'ko'); hold on
% plot(Meas_Temp2,Meas_Je2,'kv'); hold on
xlim([900 1600])
ylim([0 1.2])
xlabel(strcat('Temperature [',deg,'C]'))
ylabel('Emission Current Density [A/cm^2]')
grid
% title({'SIMULATED ACTIVITY CURVES';[num2str(d_in),'" Gap, ',num2str(V),' V,
',num2str(n),' Holes, ',num2str(dia),'" Dia']})

% figure
% subplot(2,1,1)
% scatter(T_c,Ie_TL)
% title({[num2str(n),' Holes, ',num2str(dia),'" Dia Holes, ',num2str(V),' V
Acc. Potential'];' ';'Steady State Emission'})
% ylabel('[A]')
% subplot(2,1,2)
% scatter(T_c,wfunc)
% ylabel('[eV]')
% xlabel(strcat('Temperature [',deg,'C]'))
% title('Effective Steady State Work Function')

% figure;
% plot(T_c,Ie_TOT1);
% figure;
% plot(T_c,Ie_TOT1a);
% figure;
% plot(T_c,alpha);
% figure;
% plot(T_c,SCL_Pct,':ok'); hold on
% title({'SIMULATED MIRAM CURVE';' ';[num2str(n),' Holes, ',num2str(dia),'"
Dia Holes, ',num2str(V),' V Acc. Potential']})
% xlabel(strcat('Temperature [',deg,'C]'))
% ylabel('Space Charge Limited Current [%]')
% legend({Current_density})
% grid

% figure;
% plot(T_c,Ie_n,'--k'); hold on
% plot(T_c,Ie_TOT2,'-.'); hold on
% refline(0,Ie_SCL2)
% xlabel(strcat('Temperature [',deg,'C]'))
% ylabel('Emission Current [A]')
% grid
```

7.4 Emission Model Child Code

```
function [Ie_TL,wfunc] = LWF_Filament_VarParam(T,dia,n,V,d)
% Bao Nguyen, 14 Dec 2017, Colorado State University

% Function Summary:
% 'LWF_Filament_VarParam' is referenced by 'LWF_Filament_VarTemp',
% 'Mod_Filament_VarHoleSize', 'Mod_Filament_VarHoleQty', &
% 'Mod_Filament_VarVolt' to analyze the surface diffusion, emissions, &
% work function of a LWF Sciaky filament over a range of temperatures,
% hole sizes, hole quantities, or voltages. '..._VarParam' is essentially
% the same as 'Mod_Filament_Baseline' with the exception that '..._VarParam'
% accepts arguments for temperature, T [K], hole qty, n, hole size, dia [in],
% voltage, V, and anode distance, d [m]. LWF_Filament_VarParam
% returns values for temperature limited emissions, Ie_TL [A], and
% effective work function, wfunc [eV].

% Function Background:
% This function uses code originally developed by Benny Rubin and John
% D. Williams for modeling the diffusion of barium onto a tungsten surface
% in a hollow cathode. Parameters associated with tungsten (work function)
% have been changed to reflect usage with tantalum. The empirically derived
% values used in Benny's code have been used in this code as well.

% Function General Solving Structure:
% Use the previously mentioned MATLAB scripts to specify ranges for
% temperature, hole size, hole quantity, or accelerating voltage/potential.
% Refer to those scripts for info on how they use '..._VarParam'. This code
% uses the MATLAB function, 'pdepe', to solve the partial differential
% equation for the surface coverage/diffusion of barium on the filament's
% planar, emitting surface. It uses parameterized functions of the pde
% ('diffusion'), boundary ('diff_bc') and initial ('diff_ic') conditions in
% specific forms along with vectors for space (radius) and time. The
% fractional surface coverage is then used to solve for the work function
% which in turn is used to solve for emission current density and then
% integrated over the emitting surface area of the filament to find the
% temperature limited emission current.

          %%%%%%%%%%%%%%%% SCRIPT CONSTANTS %%%%%%%%%%%%%%%%

m = 1;                      % geometry parameter for 'pdepe' function

% Physical constants
k = 1.3806503e-23;          % Boltzmann constant [J/K]
q = 1.6e-19;                % elementary charge [C]
m_q = 9.109e-31;            % elementary charge mass [kg]
A = 1.20173e6;              % Richardson's constant [A/(m^2*K^2)]
e0 = 8.854e-12;             % vacuum permittivity [F/m]
Gr = 0.50;                  % reflection coefficient [-]
phi_ta = 4.22;              % work function, Tantalum [eV]
phi_ba = 2.49;              % work function, Barium [eV]

% Empirical constants from Benny's code
G = 2.5166;                 % gamma determined from Fig. 2 in Longo, 1984
D0 = 9e-6;                  % pre-exp constant, surface diffusion [m^2/s]
Ed = 0.6918;                % activation energy, diffusion [eV]
```

```
t0 = 2.131e6;                % pre-exp constant, desorption time [1/s]
Et = 2.06;                   % activation energy, desorption [eV],
                             % same as in boundsurfcov_steady.m

  %%%%%%%%%%%%% DIFFUSION, EMISSION, & WORK FUNCTION SOLVER %%%%%%%%%%%%%

% Divide filament surface area equally among number of holes and find the
% radius, r_h, associated with the "hole" area. This division is obviously
% an approximation as there will be "gaps" between each "holes" area. This
% radius, r1, will be doubled in vector, r, for use in
r0 = (dia/2)*0.0254;         % hole radius [m]
r_f = 2.22e-3;               % filament surface radius (0.175" dia.) [m]
A_f = pi*r_f^2;              % filament surface area [m^2]
A_h = A_f/n;                 % fictional filament surface area per hole [m^2]
r_h = sqrt(A_h/pi);          % fictional filament surface radius per hole [m]

% Radial (spacial) grid for twice the fictional hole radius. 2*r_h is used
% as outer boundary to evaluate diffusion to avoid boundary condition on
% outer boundary of fictional filament surface radius
rsteps = 200;                % radial grid resolution (default: 200)
dr = (r_h-r0)/rsteps;        % radial spacing ("delta r") for integration
r = linspace(r0,2*r_h,rsteps);

% Temporal grid
t_end = 60;                  % duration of simulation [s]
tsteps = 2000;               % temporal grid resolution (default: 2000)
t = linspace(0,t_end,tsteps);

% Spacial and temporal plotting vectors. First columns are associated with
% boundary and initial conditions and are removed for plot clarity
% r_c = r(2:rsteps);
% t_c = t(2:tsteps);

% Solve transient diffusion eqn for fractional surface coverage, theta. Cut
% off first column of theta (theta_c) where surface coverage associated
% with boundary condition is equal to 1
theta = pdepe(m,@diffusion,@diff_ic,@diff_bc,r,t);
% theta = zeros(tsteps,rsteps);       % optional 0% barium coverage (pure Ta)
% theta_c = theta(:,2:rsteps);

% Find the theoretical work function, phi [eV], based on fractional surface
% coverage. Cut off first row of phi (phi_c) where work function is
% associated with initial condition
phi = phi_ta*(G*phi_ta/phi_ba).^(G*theta/(1-G))+phi_ba*(1-
(G*phi_ta/phi_ba).^(theta/(1-G)));
% phi_c = phi(2:tsteps,:);

% Solve the Richardson-Dushman equation with the Schottky enhancement term
% for the temperature limited emission current density, Je_TL [A/m^2]. The
% Schottky value that has been commented out is the estimated value used in
% the plasma-immersed testing set-up which has been superseded by the
% vacuum set-up.
Schottky = exp((q/(k*T))*sqrt((q*V)/(4*pi*e0*d)));
Je_TL = A*Gr*(T^2)*exp((-q*phi)/(k*T))*Schottky;
% Je_c = Je(:,2:rsteps);

% Truncate Je and r over the radial grid to boundary of the fictional
```

```
% filament surface radius. This effectively cuts off the current density
% beyond r_h.
Je_t = Je_TL(:,1:length(r(r<=r_h)));
r_t = r(1:length(r(r<=r_h)));

% Integrate Je_t over the fictional filament surface radius, r_h for
% TL emission current, Ie [A], over the range of the temporal grid for a
% single hole. Multiply by the total number of holes, n, to estimate the
% total emission over the filament's emitting surface.
Ie_single = pi*Je_t*r_t'*dr;                % [A]
Ie_n = n*Ie_single;                         % [A]

% Using the TL emission current, Ie_n [A], back-calculate for the
% "effective" work function, phi_eff [eV]
ZFe = Ie_n./(A_f*Schottky);                 %Zero-field saturated emission
phi_eff = ((-k*T)/q)*log(ZFe/(A*Gr*(T^2)));

       %%%%%%%%%%%%%%%% FUNCTION RETURN VALUES %%%%%%%%%%%%%%%%

% Select the last term in the temporal grid for TL emissions and effective
% work function as the steady state values.
Ie_TL = Ie_n(end,:);                        % [A]
wfunc = phi_eff(end,:);                     % [eV]

        %%%%%%%%%%%%%%%% PARAMETERIZED FUNCTIONS %%%%%%%%%%%%%%%%

%-------------------------------------------------------------------------
function [c,f,s] = diffusion(x,t,u,DuDx)
% Establishes diagonal matrix, c, flux term, f, and source term, s, for use
% in function 'pdepe'. Terms are based on transient continuity eqn for
% surface diffusion and desorption. Flux term, f, is associated with the
% surface diffusion term, D. Source term, s, is associated with the
% desorption term, theta^5/tau, or the barium monolayer evaporation rate
% (Jensen et al, eqn 5)
    c = 1;
    f = D0*exp((-q*Ed)/(k*T))*DuDx;
    s = t0*exp((-q*Et)/(k*T))*u^5;
end
%-------------------------------------------------------------------------
function u0=diff_ic(x)
% Establishes initial condition term, u0, for use in function 'pdepe'
    u0 = 0;
end
%-------------------------------------------------------------------------
function [p1,q1,pr,qr]=diff_bc(x1,ul,xr,ur,t)
% Establishes boundary condition terms pl (left) and pr (right) for use in
% function 'pdepe'. It first solves the transient continuity equation for
% fractional surface coverage, theta_0, for an equilbrium condition. This
% result is applied as the left boundary condition.
    theta_0 = bcond_steady(T);
    p1 = ul - theta_0;
    q1 = 0;
    pr = ur;
    qr = 0;
end
%-------------------------------------------------------------------------
end
```

7.5 Emission Model Boundary Conditions Code

```
function theta_0 = bcond_steady(T)
% Solves continuity equation for surface coverage at equilibrium condition
% ("steady") for use as boundary condition. Uses Rittner et al, eq 7, for
% barium partial pressure, P, in mm Hg and T is expressed in kelvin.

%Constants
k = 1.3806503e-23;                  % Boltzmann constant [J/K]
q = 1.6e-19;                        % elementary charge [C]
M_ba = 1.66e-27*137.327;            % mass, Barium (mass in amu*amu) [kg]
R_ba = 2.15e-10;                    % atomic radius, Barium [m]

%Empirical contants from Benny's code
t0 = 2.131e6;                       % pre-exp constant, desorption time [1/s]
Et = 2.06;                          % activation energy, desorption [eV],
                                    % same as in boundsurfcov_steady.m

%Conversion units
mmHg_Pa = 133.3;                    % mm mercury to pascal

theta_0 = fzero(@diff_bc,0);

%-------------------------------------------------------------------------
function f = diff_bc(th)
%     P = 10^(-20360/T+8.56)*mmHg_Pa;   %Rittner et al (1957) Eqn 7. [Pa]
    P = 16.475*exp(-18538/T);
    tau = t0*exp((-q*Et)/(k*T))*th^5;
    ka = 2*R_ba^2*P*sqrt(1/(k*T*M_ba));
    f = ka*(1-th)-tau;
end
%-------------------------------------------------------------------------
end
```